Early Measurement of the Top Quark Mass at the ATLAS Experiment

Diplomarbeit an der Fakultät für Physik
der
Ludwig-Maximilians-Universität München

vorgelegt von

Klaus Herrmann

geboren in München

München, den 31. März 2009

1. Gutachter: Prof. Dr. Otmar Biebel
2. Gutachter: Prof. Dr. Martin Faessler

Zusammenfassung

Am Large Hadron Collider (LHC) werden ab diesem Jahr Proton-Proton-Kollisionen bei einer Schwerpunktsenergie von 10 TeV stattfinden, bei denen Top-Antitop-Paare mit einem Wirkungsquerschnitt von ca. 400 pb erzeugt werden. Dabei soll im Laufe der ersten Datennahme eine integrierte Luminosität von $\int \mathscr{L} \mathrm{d}t = 200\,\mathrm{pb}^{-1}$ erreicht werden.

Im Rahmen dieser Studie wird gezeigt, dass unter den Bedingungen der ersten Datennahme, insbesondere trotz einer noch unvollständigen Kalibration des ATLAS-Detektors, eine Wiederentdeckung des Top-Quarks und eine frühe Bestimmung seiner Masse möglich sind. Dazu wird ein Szenario mit relativ geringer integrierter Luminosität ($\int \mathscr{L} \mathrm{d}t = 100\,\mathrm{pb}^{-1}$) betrachtet, mit einer angenommenen Unsicherheit von 10% auf die Jet-Energieskala und ohne die Verwendung von b-tagging.

Aufgrund des geringen Datenvolumens wird ein künstliches neuronales Netz im Rahmen der Ereignisrekonstruktion eingesetzt, wodurch die Signifikanz des Signals im Vergleich zu einer schnittbasierten Methode um mehr als 30% steigt. Die Bestimmung der Masse des Top-Quarks erfolgt im semileptonischen Zerfallskanal, wobei die 3-Jet- und 2-Jet-Massen, entsprechend den Massen von Top-Quark und W-Boson im hadronischen Zerfall, einzeln bestimmt werden. Um einen möglichen Skalierungsfaktor für die Jet-Energien und -Impulse in frühen Messdaten herauszukürzen, wird die Top-Quarkmasse mit der von der Particle Data Group angegebenen W-Masse, $m_{\mathrm{W,PDG}} = 80.4\,\mathrm{GeV}$, skaliert. Dies geschieht durch die Berechnung von

$$m_{\mathrm{top}} = \frac{m_{3-\mathrm{jet}}}{m_{2-\mathrm{jet}}} \cdot m_{\mathrm{W,PDG}}.$$

In diesem Szenario ergibt sich eine Unsicherheit von

$$\frac{\Delta m_{\mathrm{top}}}{m_{\mathrm{top}}} = \pm 3.6\%\,(\mathrm{stat}) \pm 1.6\%\,(\mathrm{JES})$$

auf die Top-Quarkmasse.

Eine frühe Bestimmung der Masse des Top-Quarks ist also mit den ersten Messdaten des ATLAS-Detektors bereits möglich. Dabei kann eine Präzision von ca. 4% erreicht werden.

Abstract

Starting this year, the Large Hadron Collider (LHC) will produce top-antitop pairs from proton-proton collisions with an estimated cross section of 400 pb at 10 TeV centre of mass energy. An estimated integrated luminosity of $\int \mathscr{L} \mathrm{d}t = 200\,\mathrm{pb}^{-1}$ will be reached in the first run of data taking.

This study shows that even under the conditions of the first run of the LHC, where the ATLAS detector is assumed to be not fully calibrated yet, a rediscovery of the top quark and an early determination of its mass is still possible. For this purpose a scenario with relatively low statistics ($\int \mathscr{L} \mathrm{d}t = 100\,\mathrm{pb}^{-1}$) is considered, and an uncertainty of 10% on the Jet Energy Scale is assumed and b-tagging is not used.

To meet the challenge of low statistics, the signal significance is raised by over 30%, compared to standard cuts, by the use of an artificial neural network in the event reconstruction. The determination of the top quark mass is performed in the semileptonic decay channel, where the masses of the W boson and top quark from the hadronic decay are determined separately as the 2-jet and 3-jet masses, respectively. To cancel out a possible scaling factor on the jet energies and momenta in early data, the top quark mass is rescaled with the W boson mass from the Particle Data Group, $m_{\mathrm{W,PDG}} = 80.4\,\mathrm{GeV}$, by calculation of

$$m_{\mathrm{top}} = \frac{m_{3-\mathrm{jet}}}{m_{2-\mathrm{jet}}} \cdot m_{\mathrm{W,PDG}}.$$

In the given scenario the resulting uncertainty on the top quark mass is estimated as

$$\frac{\Delta m_{\mathrm{top}}}{m_{\mathrm{top}}} = \pm 3.6\%\,(\mathrm{stat}) \pm 1.6\%\,(\mathrm{JES}).$$

Hence a first measurement of the top quark mass is indeed possible with the first data taken at the ATLAS detector, and a precision of about 4% is achievable.

Contents

Chapter 1

Introduction

The Large Hadron Collider (LHC) at the European Organisation for Nuclear Research (CERN) will start its operation this year. As a proton-proton collider with an unprecedented centre-of-mass energy of 14 TeV, more than seven times higher than the highest collision energy reached so far, it will allow an experimental exploration of physics under conditions similar to the universe very shortly after the Big Bang. The origin and structure of matter can be studied at the tera electron volt (TeV) energy scale for the first time, a huge step forward for the field of particle physics.

The Standard Model of particle physics is the theory that describes the properties and interactions of the fundamental constituents of matter, the quarks and leptons. It is a consistent theory, and has withstood all experimental tests at previous collider experiments. Nevertheless, research in this area is far from complete: The Higgs boson, an interaction particle predicted by the Standard Model, has yet to be found – the LHC will either do so, or disprove the theory in its current form. And in any case, the Standard Model describes some phenomena exceptionally well but fails to explain their origin. Several extensions to the model that attempt to shed light on the causes of these phenomena have thus been proposed, like Extra Dimensions and Supersymmetry to name two popular examples. Much work has been done at Fermilab's Tevatron collider already, but at the LHC these theories can finally be subjected to experimental tests at the TeV energy scale.

An ongoing field of research is the top quark: It is by far the heaviest elementary particle, with a peculiarly high mass of $m_{\text{top}} = 173.1 \pm 1.3\,\text{GeV}$ [1], close to the scale of electroweak symmetry breaking. Because of its great mass it has only been detected at the CDF and D0 experiments at the Tevatron so far. Many of its properties could not be satisfactorily determined yet, and the top quark might well play a more fundamental role in the interactions of particles than it is currently assumed. Although the uncertainty on the top quark mass is smaller than 1% already, an even more precise measurement of its mass will provide a test for the Standard Model and assist the search for the Higgs boson.

This thesis, however, presents a method not for a precision measurement but for an early determination of the top quark mass with the ATLAS detector at the LHC; the aim is to achieve a rediscovery of the top quark with the very first data taken at ATLAS, and to perform a first mass measurement with a detector that has not been fully calibrated yet. Based on simulations for the particle interactions and their corresponding detector response, the study shows that a measurement of m_{top} with a precision of about 4% is possible with an integrated luminosity of $\int \mathscr{L}\,\text{d}t = 100\,\text{pb}^{-1}$, a value that will be reached during the first run of the LHC.

Chapter 2

Theory

2.1 The Standard Model of Particle Physics

The so-called *Standard Model* of particle physics is a consistent theory describing the elementary particles as the fundamental constituents of matter and their interactions via the electromagnetic, weak and strong forces with their corresponding exchange particles. The fourth elementary force, gravity, is not covered by the model.

2.1.1 Fermions

Fermions are defined as particles with spin 1/2 and are split into two subgroups: leptons and quarks. Both can be divided further into three generations, but only the particles of the first generation are stable and form ordinary matter, with up and down quarks being the constituents of the protons and neutrons of atomic nuclei, and electrons filling the shell. Particles of the second and third generations can be produced and observed at collider experiments with high energies but decay after a short lifetime. Table 2.1 lists the leptons in the Standard Model, Table 2.2 the quarks. Anti-particles exist for all twelve fermions, which are written as $\bar{\mathrm{q}}$ and $\bar{\ell}$ for quarks and leptons, respectively, and have opposite charge-type quantum numbers.

Generation	Lepton	Symbol	Charge [e]	Mass [GeV]
1	electron	e	-1	$511 \cdot 10^{-6}$
	electron neutrino	ν_e	0	$< 2.2 \cdot 10^{-9}$
2	muon	μ	-1	$105.7 \cdot 10^{-3}$
	muon neutrino	ν_μ	0	$< 170 \cdot 10^{-6}$
3	tau	τ	-1	1.777
	tau neutrino	ν_τ	0	$< 15.5 \cdot 10^{-3}$

Table 2.1: Leptons in the Standard Model (with masses from [2]).

Generation	Quark Flavour	Symbol	Charge [e]	Mass [GeV]
1	up	u	$+\,2/3$	0.00225 ± 0.00075
	down	d	$-\,1/3$	0.005 ± 0.002
2	charm	c	$+\,2/3$	1.27 ± 0.11
	strange	s	$-\,1/3$	0.104 ± 0.034
3	top	t	$+\,2/3$	173.1 ± 1.3
	bottom	b	$-\,1/3$	4.20 ± 0.17

Table 2.2: Quarks in the Standard Model (with masses from [1] and [2])

2.1.2 Bosons

The *force carrier bosons* or *gauge bosons* are spin one particles that mediate the fundamental forces of interaction, namely the electromagnetic, weak and strong forces (see Table 2.3). The photon is the exchange particle of Quantum Electrodynamics (QED), the theory of the electromagnetic force. It couples to charged particles and has an infinite range as it is massless. $W^{\pm}$ and Z^0 are massive bosons (with masses $m_W = 80.4\,\text{GeV}$ and $m_Z = 91.2\,\text{GeV}$ [2]) mediating the weak interaction, which affects all fermions and ranges over short distances only. The fact that the $W^{\pm}$ is electrically charged allows it to also couple to the photon. A unified theory allows the combination of photons, $W^{\pm}$ and Z^0 to a so-called electroweak interaction.

Interaction	Range [m]	Gauge Boson	Quantum Number
Electromagnetism	∞	photon (γ)	electric charge
Weak Force	$\ll 10^{-16}$	$W^{\pm}$, Z	weak isospin
Strong Force	$10^{-15} - 10^{-16}$	gluon (g)	colour charge

Table 2.3: The elementary interactions

The strong force is mediated via gluons that couple to colour-charged particles. These are the quarks and the gluons themselves. The theory of Quantum Chromodynamics (QCD) describes this kind of interaction, which is limited in range due to the gluons interacting with each other.

2.1.3 Electroweak Couplings

The electroweak theory is a quantum field theory based on the gauge principle, i.e. the invariance of the equations describing particle interactions under local gauge transformations. The local symmetry of the electroweak force is represented by a $U(1) \otimes SU(2)$ group, and the need for spin one gauge bosons as quantised mediators of the interaction, and the phenomena of electric charge and weak isospin for the U(1) and SU(2) symmetry, respectively, are consequences of the theory. Calculations are done perturbatively with the so-called Feynman calculus [3].

However, the symmetry only holds for massless gauge bosons and is broken as the $W^{\pm}$ and Z have a non-zero mass. That leads to a separate description of the electromagnetic force with photons as exchange particles and electric charge as the corresponding quantum number and of the weak interaction with the $W^{\pm}$ and Z^0 gauge bosons and the weak isospin.

The fundamental couplings between the gauge bosons of the electromagnetic and weak interactions and fermions are shown in Figure 2.1 with Feynman diagrams, the standard visualisation for particle interactions. These represent a space-time coordinate frame with a horizontal time axis and a vertical space axis in which the interaction vertices are illustrated.

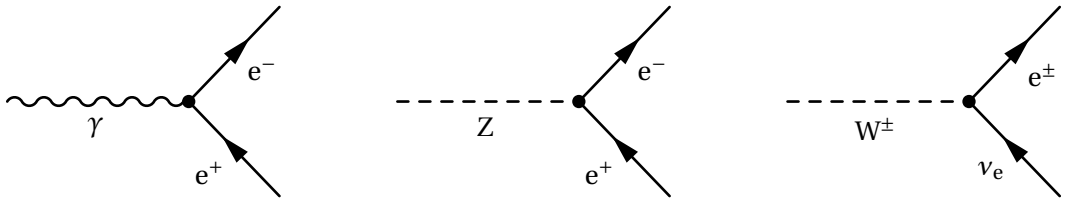

Figure 2.1: Feynman diagrams of the fundamental electroweak boson-fermion couplings

2.1.4 Quantum Chromodynamics

As mentioned before, another quantum field theory is needed to describe the strong interaction: the theory of Quantum Chromodynamics. It is mediated via gluons and knows three different *colour charges* and their corresponding anti-charges. Quarks couple to the strong interaction as they carry colour charge in addition to the electric charge, but a major difference to the electromagnetic force is that the gauge bosons are charged themselves, too – the gluons carry a colour anti-colour charge pair – which allows gluons not only to couple to quarks but to each other as well, a phenomenon called *gluon self coupling*. The Feynman diagrams for the basic couplings are shown in Figure 2.2. The charges are labelled r, g and b ($\bar{r}, \bar{g}$ and $\bar{b}$ for the anti-charges). The interaction is represented by a SU(3) symmetry group, giving the full Standard Model gauge field a U(1) ⊗ SU(2) ⊗ SU(3) symmetry.

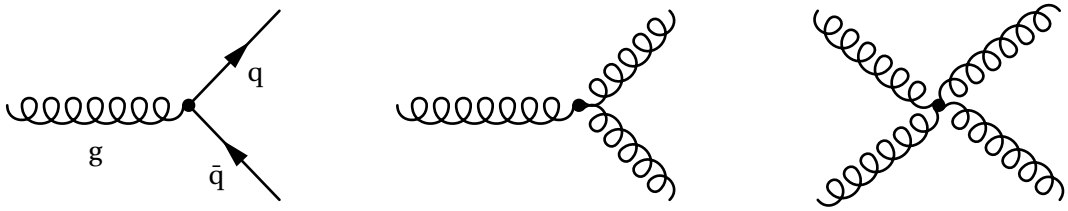

Figure 2.2: Feynman diagrams of the basic quark-gluon and gluon-gluon vertices

The three different types of colour charge give rise to the existence of every quark flavour in all three colours. This is necessary to explain for example the cross section ratio of $e^+e^- \to \mu^+\mu^-$ and $e^+e^- \to q\bar{q}$, and to satisfy the Pauli exclusion principle for the Ω^- particle consisting of three strange quarks.

The strength of the strong interaction is expressed with the coupling "constant" α_S, which depends on the energy scale and therefore on the distance between colour charged particles. Because of the gluon self coupling α_S approaches zero for high momentum transfers, allowing for free movement of quarks and gluons at low distances (called *asymptotic freedom*); perturbative calculations are possible in this regime. However, towards low momentum transfers the perturbation theory breaks down and a phenomenon called *colour confinement* is visible: an observation of free quarks is impossible, and α_S increases.

2.1.5 Hadronisation

Due to the colour confinement, quarks can only exist as *partons* inside colour neutral bound states called hadrons. After a scattering process with single quarks or gluons in the final state, new quark anti-quark pairs arise due to vacuum polarisation in the gluon field between the original quarks or gluons. New particles are created until all partons are bound into hadronic states, which are either mesons (quark anti-quark states), or baryons (three quark states), resulting in a so-called *hadronic jet*. This transformation process is called *hadronisation* (see Figure 2.3) and can only be modelled phenomenologically since perturbative calculations in the regime of quark confinement are not possible.

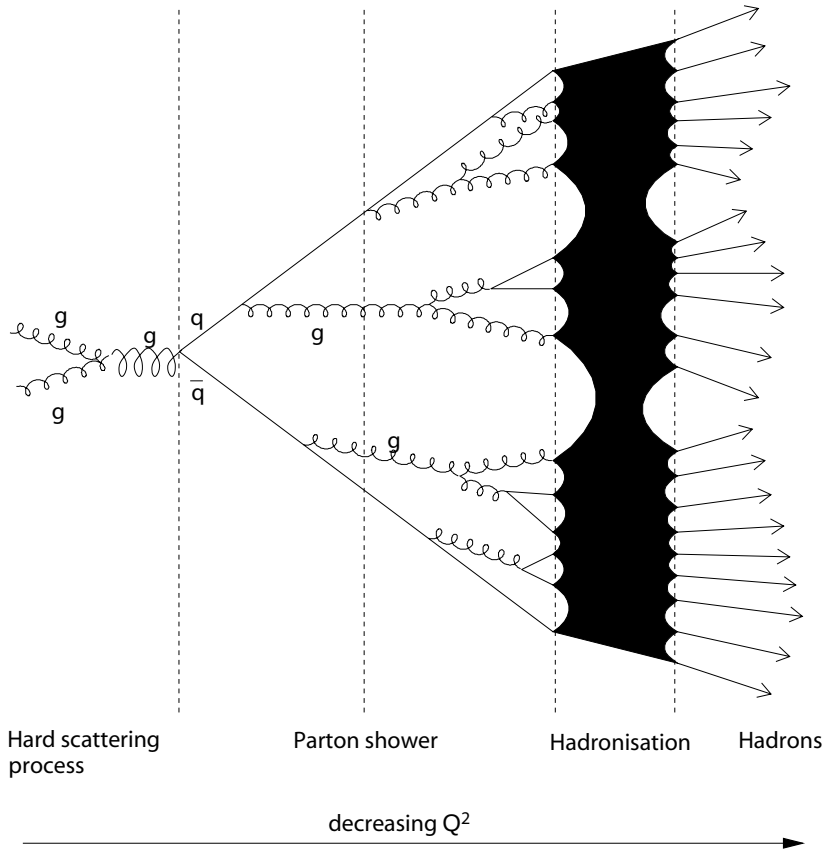

Figure 2.3: Quarks and gluons are transformed into hadrons in the process of hadronisation (Q is the energy scale)

2.2 The Top Quark

The top quark, first proposed as the weak isospin partner of the bottom quark in 1977 [4], was finally discovered in 1995 at the CDF and D0 experiments at Fermilab [5,6]. It has an outstandingly high mass of over 170 GeV compared to a mass of about 5 GeV for the b quark, the next lightest quark. Its lifetime of about $5 \cdot 10^{-25}$ s [2] is shorter than the timescale of hadronisation (about

10^{-23} s), making it the only quark to not form bound states but to instead decay almost instantly.

It has a weak isospin of $+1/2$ and an electric charge of $+2/3$ like the up and charm quarks of the first and second generation. The most precise estimate of its mass is currently given as 173.1 ± 1.3 GeV [1], determined from combined results of CDF and D0.

As the top quark has so far only been discovered at the CDF and D0 experiments at the Tevatron accelerator at Fermilab, an independent discovery and mass measurement at another collider experiment is certainly desirable. The ATLAS experiment at the LHC will achieve this goal very soon after its start, as is shown in this analysis.

2.2.1 Top Pair Production at Hadron Colliders

Even though single top quarks can be produced via the weak interaction, top pair production via the strong interaction is the dominant mechanism, either via quark anti-quark annihilation or via gluon fusion (see Figure 2.4). At the LHC with its high centre-of-mass energy proton-proton collisions, gluon fusion is preferred, accounting for roughly 90% of the produced $t\bar{t}$ pairs [7]. This is due to the fact that anti-quarks only occur in fluctuations. In contrast, the annihilation process is dominant at the Tevatron where protons collide with anti-protons and, consequently, plenty of anti-quarks are present in the scattering process.

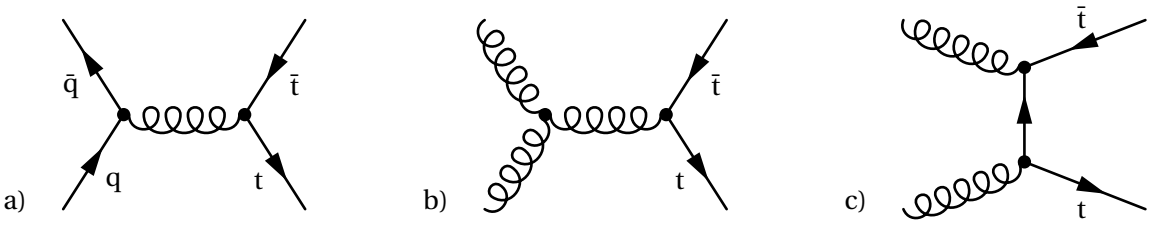

Figure 2.4: Top anti-top pairs production via quark anti-quark annihilation (a) and gluon fusion (b, c)

For the LHC operating at the planned centre-of-mass energy of $\sqrt{s} = 14$ TeV, the total top pair production cross section is estimated at about 870 pb [7]. For the lower centre-of-mass of $\sqrt{s} = 10$ TeV in the first run (see Section 4.1), this value changes to [8]

$$\sigma(\mathrm{pp} \to \mathrm{t\bar{t}}) \approx 400\,\mathrm{pb}.$$

2.2.2 Decay Modes

Top quarks almost exclusively decay into a W boson and a bottom quark:

$$\mathrm{t} \to \mathrm{W}^+ + \mathrm{b}$$

$$\bar{\mathrm{t}} \to \mathrm{W}^- + \bar{\mathrm{b}}$$

The W boson can decay leptonically, i.e. into a lepton plus a neutrino, with a branching ratio of $1/3$, or hadronically, i.e. into a quark antiquark pair, with a branching ratio of $2/3$. That leads to three categories for $t\bar{t}$ pair decays: fully leptonic, semileptonic and fully hadronic, according to the decay modes of the two W bosons. Figure 2.5 illustrates the possible combinations; more details are given in Section 4.2.

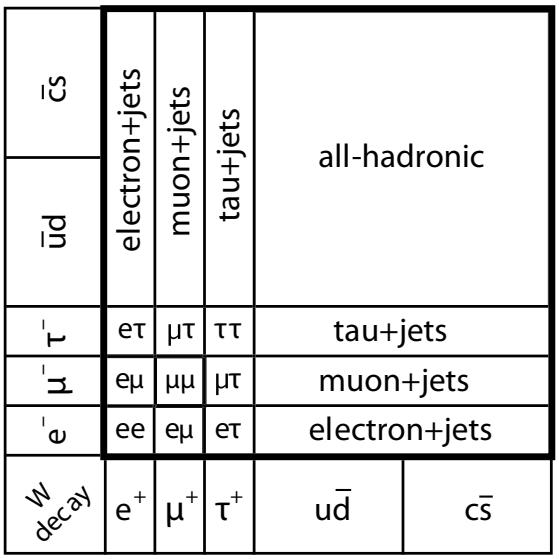

Figure 2.5: The top pair decay modes

2.2.3 The Importance of Top Quark Physics

The fact that top quark is the only particle in the Standard Model with a mass close to the scale of electroweak symmetry breaking (and is by far heavier than all other fermions) is reason enough to study top quark physics in greater detail. The properties of the top quark serve as a crucial test for the Standard Model. In addition, the reason for its high mass has yet to be understood, and a more fundamental role of the top quark in the mechanism of the electroweak symmetry breaking is possible.

Another reason for precise measurements of the top quark mass and production cross section is that top quark pair decays are an important background process for a lot of searches for physics beyond the Standard Model and hence need to be well understood. In addition, top quark physics might itself have the potential to discover new physics, e.g. with yet unknown couplings to the top quark, anomalous top quark decays or $t\bar{t}$ resonances with high masses.

Furthermore the top quark mass, together with the mass of the W boson, acts as a constraint on the mass of the Higgs boson, which has been postulated as the exchange particle of a field that gives rise to the masses of elementary particles. A precise measurement narrows the mass region in which a Higgs boson can be found according to the Standard Model; and if the Higgs boson actually exists and is detected, cross checks between the particle masses can be performed to validate the Standard Model.

Chapter 3

The ATLAS Experiment

Experimental tests of the Standard Model (see Section 2.1) are carried out with collider experiments. Even though all results from such experiments have so far confirmed its predictions, open questions remain. Most importantly the Higgs boson, which is needed to complete the model, has not yet been detected.

The Large Hadron Collider (LHC) is a new proton-proton collider experiment at the European Organisation for Nuclear Research (CERN), due to start operation this year. With a centre-of-mass energy of 14 TeV, one order of magnitude higher than the maximum energy reached at other experiments so far, physics at the TeV mass scale can be explored, allowing for a study of the electroweak symmetry breaking, for an experimental test of the Higgs mechanism, and for a search for phenomena beyond the Standard Model.

3.1 The Large Hadron Collider

The LHC is installed into the tunnel previously used for the CERN LEP electron positron collider. This tunnel is almost 27 km long, and lies between 45 m and 170 m beneath the surface [9]. It is located at the border between France and Switzerland, near Geneva.

An overview of the LHC accelerator complex is pictured in Figure 3.1. Protons from the ionisation of hydrogen are accelerated in several stages, then injected into the final pre-accelerator, the Super Proton Synchrotron (SPS), and finally into the LHC ring. At full operation, the counter-rotating beams will have an energy of 7 TeV each, resulting in a centre-of-mass energy of 14 TeV. The limiting factor on the beam energy is strength of the superconducting beam bending magnets. To reach a high collision rate, the beams are collimated to bunches of 10^{11} protons with a bunch spacing of 25 ns. In effect, 40 million bunch crossings will take place per second, with an average of about 23 proton-proton collisions per crossing. The resulting instantaneous luminosity is $\mathscr{L} = 10^{34}\,\mathrm{cm}^{-2}\mathrm{s}^{-1}$ [9]. At a later stage, a run with heavy lead ion collisions will also be performed at a luminosity of $\mathscr{L} = 10^{27}\,\mathrm{cm}^{-2}\mathrm{s}^{-1}$ [9].

However, the accelerator will not start its operation at full energy and luminosity. A scenario for the performance expected for the first data taking is given in Section 4.1.

Four independent experiments detect the particles created in the collisions: ATLAS (see Section 3.2) and CMS [10], two general purpose detectors; LHCb, a detector focused on heavy flavour physics and the CP violation [11]; and ALICE, an experiment studying heavy ion collisions [12].

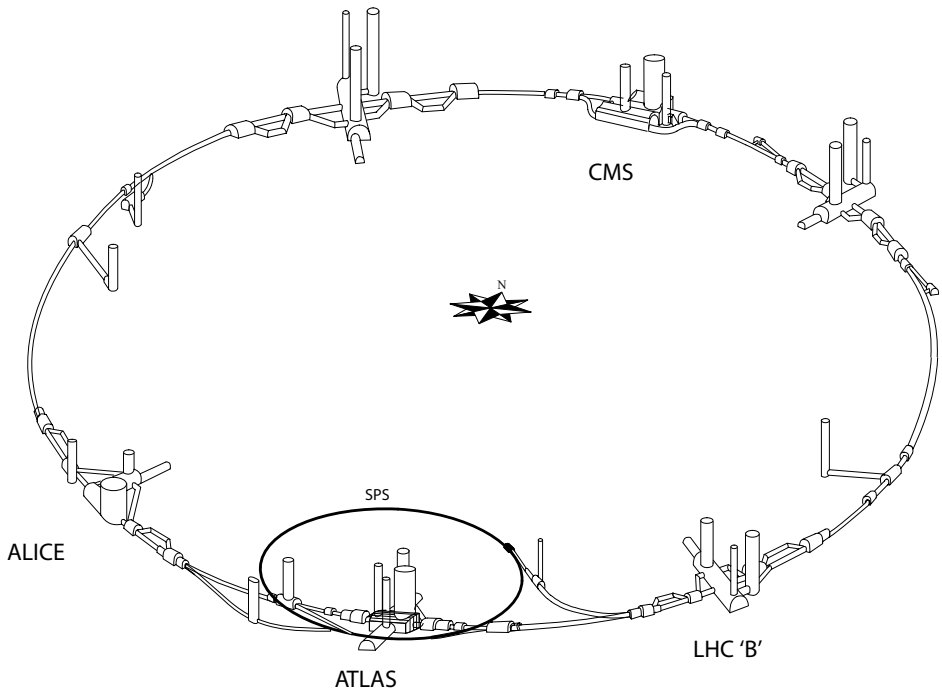

Figure 3.1: The LHC accelerator complex

3.2 The ATLAS Detector

The ATLAS detector ("A Toroidal LHC Apparatus") is the biggest detector at the LHC: it is 44 m long, 25 m high and has an overall weight of about 7000 tons. Several different components are installed in layers around the point of interaction, forming a barrel shape. These components serve different purposes in the experiment, detecting different types of particles and varying in spatial and energy resolution. Figure 3.2, a cut-away view of the detector, shows that all subsystems of the detector are divided into the barrel and end cap regions.

3.2.1 Coordinate System

In the right handed ATLAS coordinate system the z-axis is aligned alongside the beam pipe, with the y-axis and x-axis pointing upwards and towards the centre of ring, respectively, from the interaction point. The detector is forward-backwards symmetric with respect to this point.

The azimuth angle Φ is defined in the x-y-plane, with $\Phi = 0$ corresponding to the positive x-axis; the polar angle θ is the angle with respect to the z-axis ($\theta = 0$ corresponding to the positive z-axis). Usually the so-called *pseudorapidity*

$$\eta = -\ln\left(\tan\frac{\theta}{2}\right)$$

replaces the polar angle because the difference between two values of η is (in good approximation) invariant under Lorentz boosts along the z-axis. The geometric distance between two objects in the pseudorapidity-azimuthal space is $\Delta R = \sqrt{\Delta\Phi^2 + \Delta\eta^2}$.

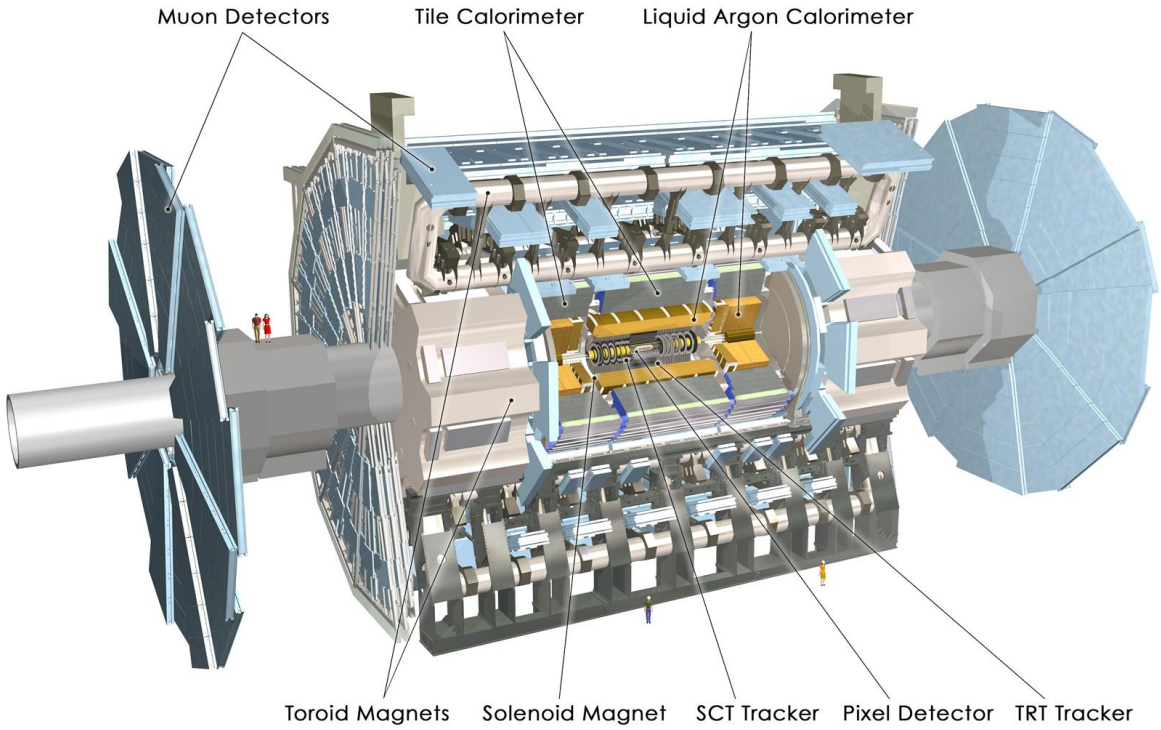

Figure 3.2: Overview of the ATLAS detector

Frequently the transverse components of energies and momenta are used, denoted as E_T and p_T, which correspond to the components vertical to the beam axis, i.e. the projections onto x-y-plane. The reason for this lies in the nature of the proton-proton collisions, which have no constant center-of-mass frame with respect to the z-axis. As a result, the particles from the hard scattering process are usually boosted along the z-axis; the transverse components of the momenta, in contrast, have to add up to zero for each event.

3.2.2 Inner Detector

The *Inner Detector* [13] is, as the name suggests, the innermost detector layer close to the interaction point and is surrounded by the central solenoid magnet. The goal of the inner detector is a precise measurement of the tracks of charged particles, and the curvature of those tracks in the 2 T magnetic field allows a determination of the momentum of electrons, muons and charged hadrons.

This is achieved with the help of three components (see Figure 3.3): The Silicon Pixel Detector and the surrounding Semiconductor Tracker (SCT) are mainly used to determine momenta, impact parameters and decay vertices; and the Transition Radiation Tracker (TRT) serves the track reconstruction and the separation of electrons and pions, using a set of tubes filled with Xenon gas.

3.2.3 Calorimeter

The calorimetric system [14], comprising the Electromagnetic Calorimeter (EM) and the Hadronic Calorimeter (HC) as shown in Figure 3.4, absorbs the energies of electrons and photons (EC) and

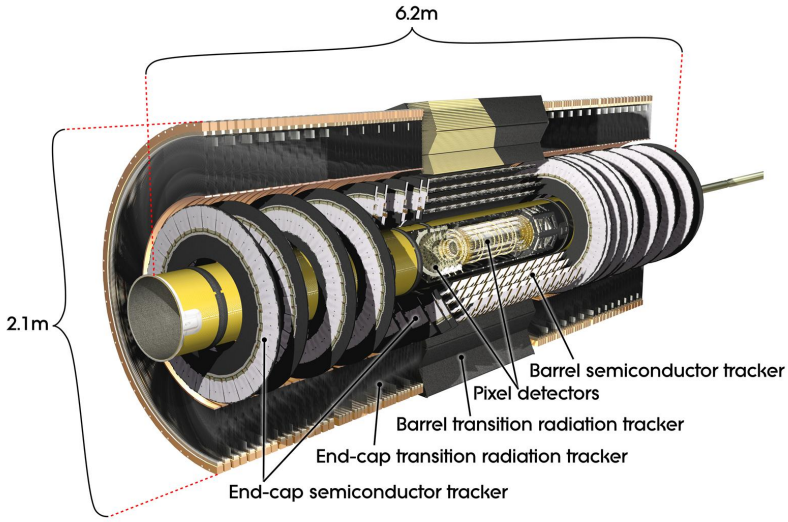

Figure 3.3: The ATLAS Inner Detector

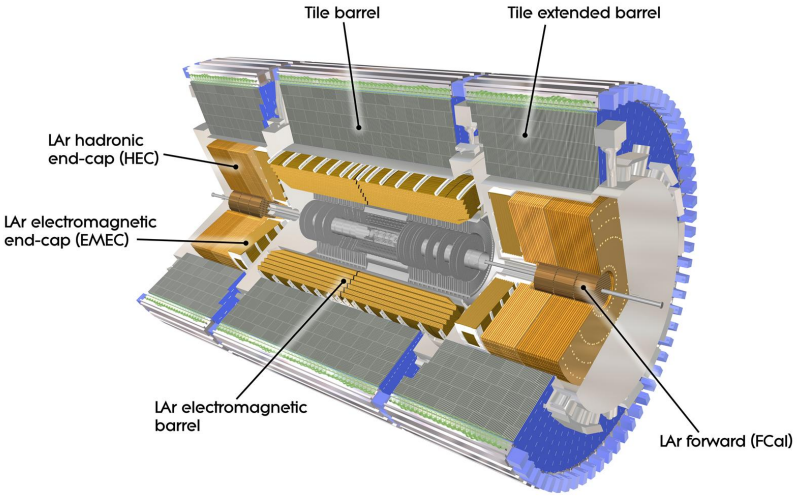

Figure 3.4: The calorimeter

hadrons (HC), respectively, allowing a measurement of these energies, and of the corresponding particles' positions.

The EM uses liquid argon (LAr) sampling calorimeters, with lead panels as absorbers, to detect the particle showers arising from the interaction of the particle with matter. Similar mechanisms are in place in the HC, using a combination of iron absorbers and scintillator plates in the central area, and absorbers made from tungsten and copper with liquid argon sampling calorimeters for the end cap components.

3.2.4 Muon System

The purpose of the Muon Spectrometer (MS) [15], the final subdetector in the ATLAS experiment, is the identification of muons and a stand-alone measurement of their positions and momenta with high precision.

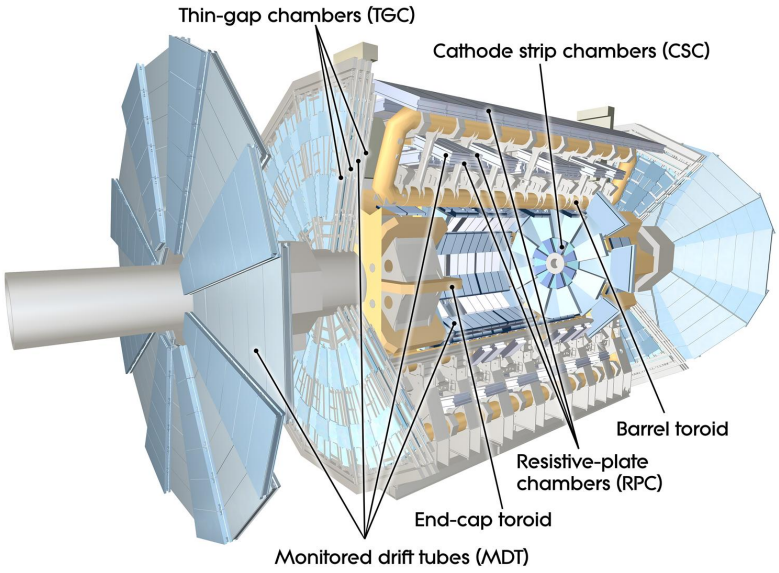

Figure 3.5: The muon system of the ATLAS detector

It consists of three layers of Monitored Drift Tube Chambers (MDTs), filled with argon and carbon dioxide (see Figure 3.5), plus Cathode Strip Chambers in the forward region. Fast trigger detectors are in place to allow for a precise timing, in the form of Resistive Plate Chambers (RPCs) and Thin Gap Champers (TGCs). The magnetic field required by the MS stems from superconducting toroid magnets and has an average strength of 0.6 T [15].

3.2.5 Triggers and Event Selection

While the collision rate at ATLAS is at 40 MHz, the event reconstruction system can only handle some 100 events per second. An efficient trigger system is therefore needed to select those events for storage that look most promising for an analysis (i.e. new physics processes, Standard Model tests etc.), and exclude for example collisions with low momentum transfer. The system used in the experiment comprises three stages:

- The hardware-based *Level-1 Trigger* (LVL1) reduces the event rate to 75 kHz by using the signals from the calorimeter and the muon system to identify bunch crossings with promising events. These events are stored in the Readout Buffer (ROB). Additionally so-called Regions of Interest (RoI) are defined, i.e. areas of the detector in which the “interesting” data describing the event can be accumulated.

- Components of the detector not included in the LVL1 trigger selection are analysed by the software-based *Level-2 Trigger* (LVL2), together with the regions of interest defined by the Level-1 trigger. The acceptance rate of this trigger is 2 kHz.

- Another software-based trigger, the *Event Filter* (EF), makes the final selection of events that are categorised and stored permanently for further analysis. The event rate is reduced to the final value of 100 Hz in this stage.

3.3 Physics Analysis at ATLAS

This analysis relies on simulated data as the LHC has not started its operation and hence no "real" data are available yet. Simulation provides a chance to test the software framework used at ATLAS, in particular the parts used for event reconstruction and physics analysis, as well as to develop strategies on how to perform the desired measurements once the experiment is running.

The software framework, ATHENA [16], is an object oriented C++ framework that serves as an abstraction layer for the raw data, providing the user with derived physics objects, e.g. in the form of four-momenta for jets and leptons. These objects are generated in the stage of event reconstruction from either simulated or real data. Furthermore, ATHENA interfaces to external tools for the simulation of physics processes and the corresponding detector responses. For an overview of the simulation and reconstruction chain see Figure 3.6.

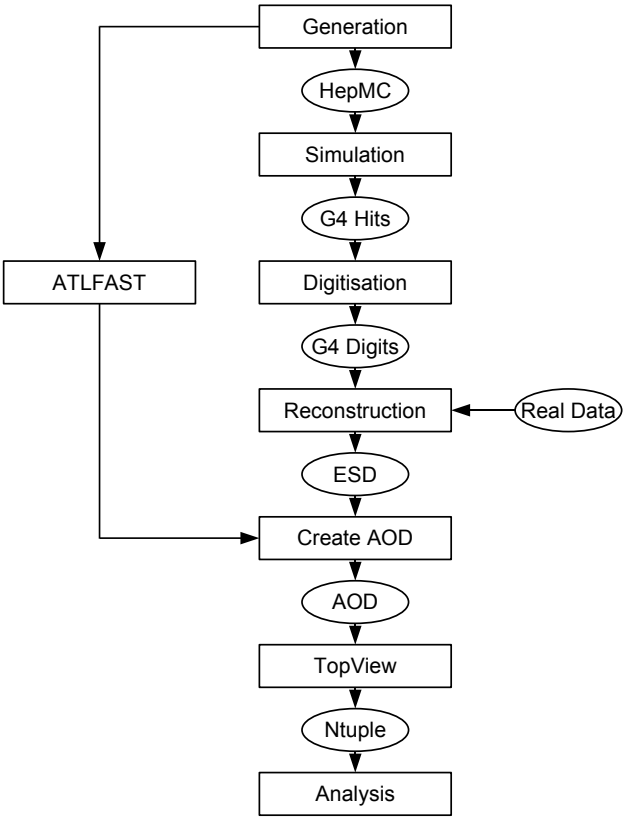

Figure 3.6: The ATLAS simulation and reconstruction chain

3.3.1 Simulation

The simulation of events comprises of three steps:

- In the *event generation* the scattering processes are simulated via Monte Carlo generators like MC@NLO [17, 18]. The following parton shower and hadronisation is modelled thereafter, using for example PYTHIA [19] and HERWIG. [20].
- The interaction with the detector material, e.g. the lead or tungsten plates in the calorimeter, is simulated with GEANT4 [21].
- Finally, in the *digitisation*, the expected detector responses are calculated, such as the drift times in the MDTs.

After these steps the simulated events correspond to the data taken by the ATLAS detector. A fast parametrised simulation, ATLFAST [22], exists that skips the second and third step of the simulation chain, as well as the first step of the reconstruction, mainly by applying a smearing on the four-momenta of the particles after the event generation.

3.3.2 Reconstruction

From the raw data the particle tracks are reconstructed, and the energies and momenta are calculated from the calorimeter responses. The resulting derived physics objects, for example the four-momenta of electrons, muons and hadronic jets, are stored in the form of Event Summary Data (ESD), usually used for calibration and optimisation of the jet reconstruction, and the less detailed Analysis Object Data (AOD) used for physics analysis.

The data in the the AOD files can be condensed into so-called ntuple files, or DPDs, which only contain the derived physics objects of interest for a specific analysis. These files are produced using tools like TOPVIEW [23], and can be read by standalone software (i.e. outside ATHENA) like the ROOT framework [24] used for this analysis.

Chapter 4

Top Quark Physics at ATLAS with Early Data

This analysis measures the mass of the top quark with the first data taken at the ATLAS detector. A scenario is considered where the LHC does not yet operate at full energy, and where the detector is not fully calibrated yet. It is assumed that $100\,\mathrm{pb}^{-1}$ of data are available for analysis after the first run, due to start in late 2009 with low luminosity.

4.1 Accelerator and Detector Performance Scenario

4.1.1 Centre-of-Mass Energy

While the LHC is planned to operate at a center-of-mass energy of $\sqrt{s} = 14\,\mathrm{TeV}$, it is likely that the experiment will start with a run at 10 TeV. This energy is used throughout the analysis unless noted otherwise.

4.1.2 Luminosity

The LHC will start with a luminosity lower than its design value ($10^{34}\,\mathrm{cm}^{-2}\mathrm{s}^{-1}$), likely in the range of $10^{30}\,\mathrm{cm}^{-2}\mathrm{s}^{-1}$. With more bunches and a higher collision rate the luminosity will increase throughout the experiment.

4.1.3 Jet Energy Scale

The energy of a hadronic jet is translated via the Jet Energy Scale (JES) from the energy of its shower measured in the calorimeter to the energy of the corresponding parton in the final state. The precision of the JES is a limiting factor on all measurements of energy and mass in hadronic processes.

While a first calibration for effects like final state radiation and imperfect jet reconstruction algorithms can be done from Monte Carlo studies, an uncertainty of about 10% can be assumed for early data. This will eventually be reduced to about 1%, but this can only be achieved through calibration with real data [25]. Well known Standard Model physics events are used for this, for

example the W and Z boson decays and the J/Ψ resonance. The fact that the JES has to be determined and calibrated separately for light quark jets and b quark jets further complicates the matter.

In the first stage of data taking this calibration will not be performed thoroughly yet. Thus not only statistical errors but also systematic deviations have to be taken into account when determining the top quark mass.

4.1.4 Leptons

In this analysis the leptons are only used as a selection criterion for $t\bar{t}$ events and the top quark mass calculation in the semileptonic channel is independent of their energy. While electron and muon identification can be regarded as unproblematic, the τ leptons' lifetime is short ($3 \cdot 10^{-13}$ s) and only its decay products can be detected. These are hard to distinguish from final state radiation and QCD background and thus not helpful for the event selection.

4.1.5 B-Tagging

Jets arising from b quarks can be separated from light quark jets as they contain hadrons with non-zero beauty with lifetimes of order 10^{-12} s that decay into many-particle final states; their decay vertices are close – in the order of millimeters – to the production vertex. If the spatial resolution of the detector is sufficient, the vertices can be resolved and the b quark jets can hence be identified; this is called *b-tagging*.

Viable b-tagging is desirable as it allows for a much better event selection of $t\bar{t}$ events with their two b quark jets. It is currently estimated that the simple b-tagging algorithms in place for early data will have an efficiency of $\epsilon_b \approx 60\%$ at a rejection rate for light quark jets ($1/\epsilon_{\text{light}}$) of 30 [26]. However, as the first real data are used for commissioning of the tagging algorithms reliance on these seems inappropriate for an early analysis.

4.1.6 Missing Transverse Energy

The missing transverse energy $\not{E}_T$ is an important part of the detector signature for the semileptonic and dileptonic $t\bar{t}$ decay channels. It is calculated either from the total energy deposits in the detector cells (with corrections for noise suppression, dead material, energy lost in the cryostats etc.) and the reconstructed muons, or from the reconstructed and classified objects [7]. Only the former is feasible in the first weeks to months as the latter requires, amongst other things, a well understood jet energy scale.

For the uncalibrated $\not{E}_T$ from the detector cells a large systematic error of 30% is to be expected [7]. So even with this method it is unlikely that a reliable measurement for values of $\not{E}_T$ as low as 20 GeV – desirable for the $t\bar{t}$ event selection – is available for early data.

4.2 Cross Sections and Detector Signatures

At a centre-of-mass energy of $\sqrt{s} = 10$ TeV the production cross section for top – anti-top pairs is about 400 pb [8] at next-to-next-to-leading order (NNLO), with a theoretical uncertainty of ca. 6%.

The cross section depends on the mass of top quark, decreasing with an increasing mass.

The top quark cannot be observed directly by the ATLAS detector: due to its short lifetime of $5 \cdot 10^{-25}$ s [2] it does not hadronise but decays directly. As a consequence only its decay products, or the jets formed during hadronisation in the case of quarks, are visible to the experiment. This is described with the *detector signature*.

4.2.1 All-Hadronic Decay Channel

The probability for both W bosons to decay into (anti-)quarks is about 4/9, so the product of branching ratio and cross section for this channel is 178 pb. With six quarks as the (only) decay products the detector signature is four light quark jets and two b quark jets; this is very hard to distinguish from QCD background, especially without a mature b-tagging mechanism in place, and thus not useful for an early analysis. In addition, a measurement in the all-hadronic decay channel is even more dependent on the JES than the other channels.

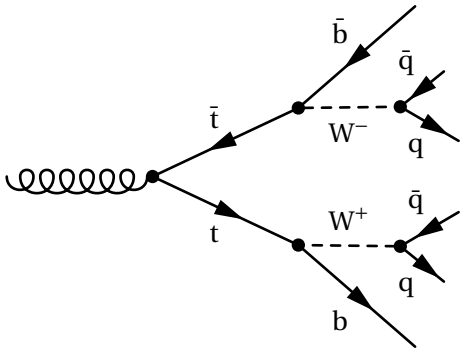

Figure 4.1: All-hadronic $t\bar{t}$ decay

4.2.2 Dileptonic Decay Channel

The dileptonic channel has a branching ratio of only 1/9 and a cross section times branching ratio of 45 pb. Two b quark jets and two leptons are visible in the detector, and the two neutrinos from the W decays lead to missing transverse energy. The two (oppositely charged) leptons allow for a very good separation from the QCD background, leading to a high signal purity. As the neutrino momenta cannot be reconstructed, sophisticated techniques like matrix element methods [27] or template methods [28] have to be used to calculate a top quark mass with this signature, and a precise measurement of $\not{E}_T$ is required.

4.2.3 Semileptonic Decay Channel

Often called the *golden channel*, the semileptonic decay channel is best suited for an early analysis. Its signature is two light quark jets, two b quark jets, one lepton, and missing transverse energy stemming from the neutrino originating from the leptonic W decay, with all jets and the lepton having relatively high transverse momenta p_T. The high-p_T-lepton is useful to separate the signal from QCD background, and the three jets from the hadronic decay allow a direct reconstruction and mass measurement of the top quark, i.e. without the use of the missing transverse energy

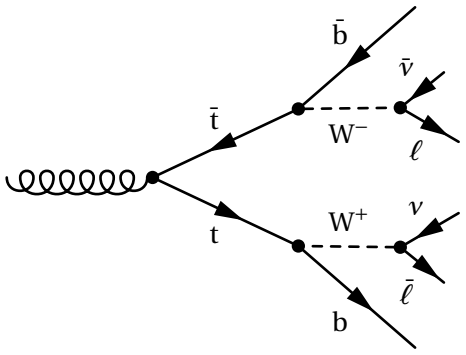

Figure 4.2: Dileptonic $t\bar{t}$ decay

from the neutrino in the leptonic decay. With a branching ratio of about $4/9$ the branching ratio times cross section (178 pb) is sufficient for an analysis with first data. If the τ-channel is excluded this value is reduced to 119 pb. Thus the measurement of m_{top} in this analysis is performed on the semileptonic channel.

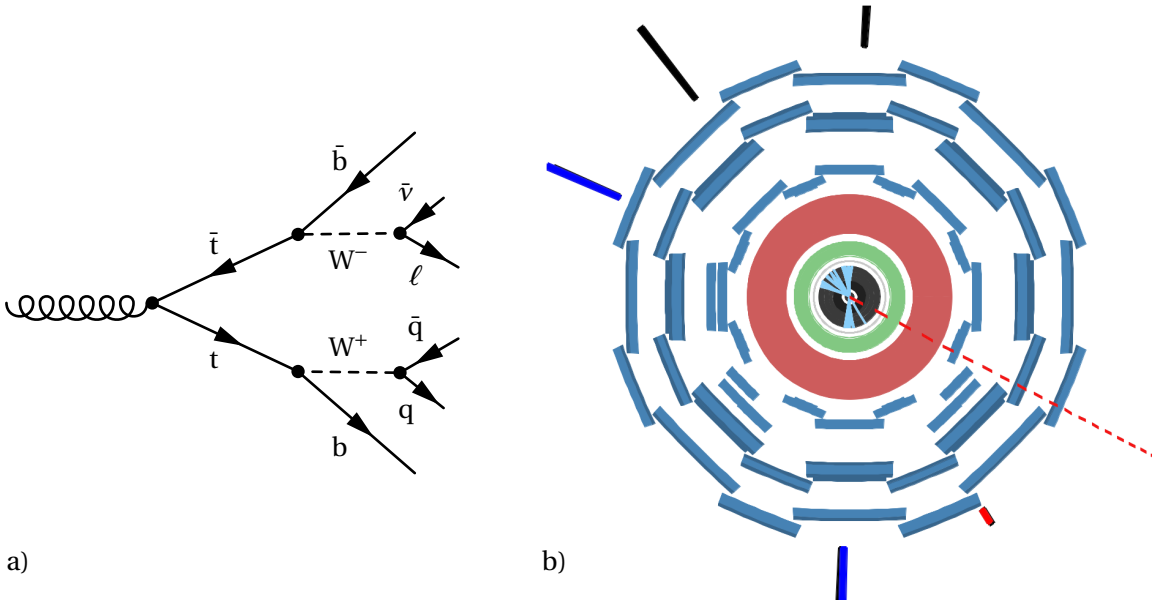

Figure 4.3: (a) Feynman diagram for the semileptonic $t\bar{t}$ decay; (b) visualisation of the detector response in the x – y-plane for a semileptonic $t\bar{t}$ event with the ATLANTIS package [29]; objects are visualised as blocks outside the detector (black: hadronic jets, dark blue: b quark jets, red: muon), the red dashed line symbolises the missing E_T, light blue lines in the centre represent tracks in the inner detector

4.3 Physical Background

Several physical processes can have a very similar or even equal detector signature to the top pair decay. A good understanding of those *background processes*, their cross sections and their properties is necessary to estimate their influence on the measurement. For the semileptonic channel the most important processes are single top production, W + Jets, and pure QCD multijet events.

4.3.1 Single Top

Single top events, produced as shown in Figure 4.4 in the *t*-channel, *s*-channel, or *Wt*-channel, can have the same objects in the final state as semileptonic $t\bar{t}$ events if the W boson decays into a lepton plus neutrino and at least one (two for the *s*-channel) additional jet arises from initial and/or final state radiation. They therefore only differ kinematically from the signal, and cannot be separated from it completely.

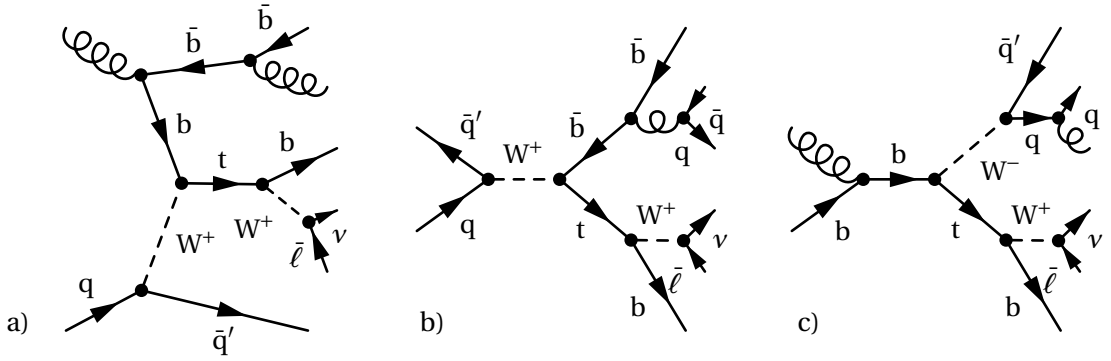

Figure 4.4: Single top production: (a) *t*-channel, (b) *s*-channel, and (c) *Wt*-channel

The calculated next-to-leading-order (NLO) cross sections for single top production at $\sqrt{s} = 10\,\text{TeV}$ and the respective branching ratios for the leptonic channel are given in Table 4.1.

channel	σ	BR (leptonic)	$\sigma \cdot$ BR (leptonic)
t-channel	125 pb	32%	40 pb
s-channel	6.6 pb	32%	2.2 pb
Wt-channel	33 pb	44%	14 pb

Table 4.1: Single top channels and their respective cross sections and branching ratios [8]

4.3.2 W + Jets

In a similar manner, leptonic decays of single W bosons form an irreducible background if at least four jets with high transverse momenta are produced through initial state radiation (see Figure 4.5). As the analysis of early data does not make use of b-tagging, these jets from associated production do not have to be b quark jets; this increases the background contribution from W + Jets significantly.

4.3.3 QCD Multijets

Pure QCD events should theoretically only resemble all-hadronic $t\bar{t}$ decays, not semileptonic ones. However, so called *non-prompt* leptons can result from weak decays inside a parton shower, particularly inside b quark jets. In the case of a large momentum transfer to the lepton the particle can be identified as an individual object.

In addition, jets can be misinterpreted as electrons if the signal in the electronic calorimeter is higher than usual, e.g. through neutral pion decays into photons. These wrongly reconstructed

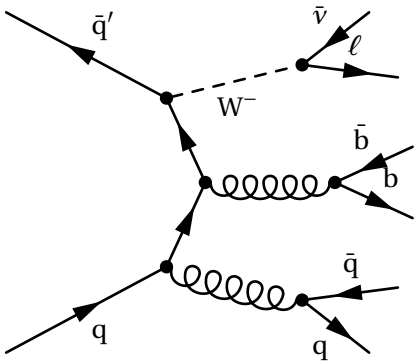

Figure 4.5: Leptonic W decays with associated jets from initial state radiation

electrons are called *fake electrons*. Even though both effects are quite rare (the fake rate is in the order of 1‰) they form a significant background to the signal because the cross section for QCD multi-jet production is several orders of magnitude higher than for top pair production.

4.4 Monte Carlo Samples

The analysis is performed using events from Monte Carlo generators for both signal and background processes. The event samples used are from the offical central production of the ATLAS collaboration.

4.4.1 Top – Anti-Top Samples

The central mass point of $m_{\text{top}} = 172.5\,\text{GeV}$ is simulated in the id-"105200" Monte Carlo Sample using MC@NLO [17,18] as the event generator and HERWIG [20] to model the parton showers. The sample includes the semileptonic and the dileptonic $\text{t}\bar{\text{t}}$ decay channels.

Additional Monte Carlo samples for different top quark mass points are available; they are used to test the stability of the method with respect to a variation of the top quark mass. These samples with their respective NNLO production cross sections at $\sqrt{s} = 10\,\text{TeV}$ according to [8] and number of events are given in Table 4.2.

Sample ID	m_{top}	σ	$\sigma \cdot$ BR (semileptonic)	N events
106203	160.0 GeV	579 pb	257 pb	59150
106201	170.0 GeV	431 pb	192 pb	58940
105200	172.5 GeV	402 pb	178 pb	482522
106202	180.0 GeV	326 pb	145 pb	59796
106204	190.0 GeV	250 pb	111 pb	58046

Table 4.2: $\text{t}\bar{\text{t}}$ samples for alternating mass points and their respective cross sections

The samples for the alternating mass points are generated using MC@NLO, too, but interfaced to PYTHIA [19] for parton showers, and make use of the ATLFAST parametrised detector simulation [22].

The next-to-leading order corrections in MC@NLO result in negative event weights for ≈ 13% of the events. The cross section at NNLO is caluclated via a multiplicative so-called k-factor of 1.06 (1.07 for the central mass point sample), which is already included in Table 4.2.

4.4.2 Physical Background Samples

The Monte Carlo samples for the single top and W + Jets events are listed in Tables 4.3 and 4.4, respectively. At the time of writing the single top sample for the s-channel with a τ in the final state was not yet available. However, with its low cross section this process is not a significant background to the semileptonic $t\bar{t}$ decay and can be omitted, especially as the semileptonic $t\bar{t}$ events with the W decaying into $\tau + \nu$ are not included in the analysis. All W + Jets samples are filtered at generator level to exclude events with less than three jets.

Sample ID	Channel	Generator	Parton Shower	$\sigma \cdot$ BR	N events
108340	t chan. $\rightarrow e+\nu$	MC@NLO	Herwig	14 pb	19750
108341	t chan. $\rightarrow \mu+\nu$	MC@NLO	Herwig	14 pb	19749
108342	t chan. $\rightarrow \tau+\nu$	MC@NLO	Herwig	14 pb	20000
108343	s chan. $\rightarrow e+\nu$	MC@NLO	Herwig	0.76 pb	3500
108344	s chan. $\rightarrow \mu+\nu$	MC@NLO	Herwig	0.76 pb	9999
105500	Wt chan.	AcerMC	Pythia	14 pb	9749

Table 4.3: Single top Monte Carlo samples

Sample ID	Channel	Generator	Parton Shower	$\sigma \cdot$ BR	N events
108240	$W \rightarrow e+\nu$ + 2 Partons	Alpgen	Herwig	183 pb	37714
108241	$W \rightarrow e+\nu$ + 3 Partons	Alpgen	Herwig	126 pb	23980
108242	$W \rightarrow e+\nu$ + 4 Partons	Alpgen	Herwig	51 pb	8500
108243	$W \rightarrow e+\nu$ + 5 Partons	Alpgen	Herwig	18 pb	3000
108244	$W \rightarrow \mu+\nu$ + 2 Partons	Alpgen	Herwig	8.3 pb	1981
108245	$W \rightarrow \mu+\nu$ + 3 Partons	Alpgen	Herwig	59 pb	9500
108246	$W \rightarrow \mu+\nu$ + 4 Partons	Alpgen	Herwig	36 pb	6313
108247	$W \rightarrow \mu+\nu$ + 5 Partons	Alpgen	Herwig	16 pb	3000
108248	$W \rightarrow \tau+\nu$ + 2 Partons	Alpgen	Herwig	75 pb	14974
108249	$W \rightarrow \tau+\nu$ + 3 Partons	Alpgen	Herwig	86 pb	17000
108250	$W \rightarrow \tau+\nu$ + 4 Partons	Alpgen	Herwig	42 pb	7927
108251	$W \rightarrow \tau+\nu$ + 5 Partons	Alpgen	Herwig	17 pb	2736
106280	$Wb\bar{b}$ + 0 Partons	Alpgen	Herwig	6.3 pb	15500
106281	$Wb\bar{b}$ + 1 Partons	Alpgen	Herwig	6.1 pb	15207
106282	$Wb\bar{b}$ + 2 Partons	Alpgen	Herwig	3.5 pb	8953
106283	$Wb\bar{b}$ + 3 Partons	Alpgen	Herwig	2.0 pb	5000

Table 4.4: W + Jets Monte Carlo samples

4.4.3 QCD Samples

At the time of writing no centrally produced QCD multi-jet samples for $\sqrt{s} = 10\,\text{TeV}$ were available. This is the case because the phase space for events with at least five jets is enormous, and with an estimated electron fake rate of about 1‰, samples with high statistics are necessary to properly estimate the influence of the QCD background on the measurements. This poses a major challange as the simulation requires a lot of computing time, even for the ATLAS collaboration with their vast resources on the LHC Computing Grid.

Because of these difficulties it is planned to estimate the height and shape of the QCD background from data once the experiment is running [30].

Chapter 5

Event Reconstruction in the Semileptonic Decay Channel

Before a measurement of the top quark mass can be conducted, the $t\bar{t}$ signal has to be separated from the physical background as far as possible. This is done by means of *preselection cuts*, that use the detector signature and kinematic properties of the events.
In a second step the "hadronic" top quark has to be reconstructed from its decay products measured in the detector, which involves finding the correct combination of jets that originate from the hadronic top quark decay. A multivariate analysis is presented for this purpose as an alternative to the standard selection based on a geometric or kinematic criterion.

5.1 Physical Background Discrimination

As the first step of the analysis, *cuts* are applied to the sample, i.e. only events that fulfill several criteria are considered for further analysis. This is done to separate the top pair decays from all other physics processes. While it is possible to significantly reduce the background, it cannot be removed completely due to the similarities in the final states of the different processes. The cuts also always remove a part of the signal, decreasing the number of events available for analysis.

5.1.1 Preselection Cuts

Choosing selection cuts always means dealing with the trade-off between signal efficiency and the level of background reduction. This is most evident for the choice of the number of jets that are required to be reconstructed in one event: While the semileptonic $t\bar{t}$ decay has four jets in its detector signature, it is not always possible to reconstruct all of those, because a jet can be located too close to the beam axis, where many particles from soft scattering processes are found, and the detector resolution is worse than in the central area. Furthermore, two jets can be emitted in a very similar direction and be reconstructed as one (especially with the cone algorithm used for jet reconstruction in this analysis, due to its infrared sensitivity [31]); or jets can have unusually low transverse momenta and be ignored. The opposite effect is just as important: additional jets that stem from initial or final state radiation often increase the number of jets in semileptonic top pair decays (but are usually lower in transverse momentum, see Figure 5.1).

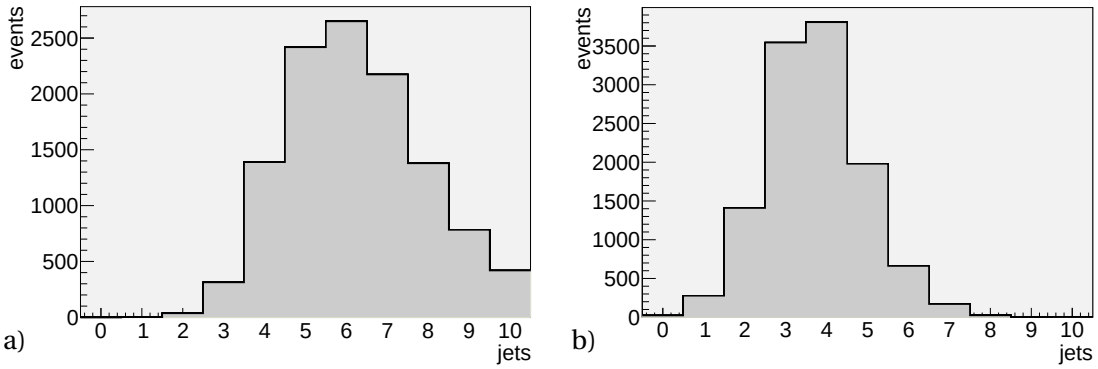

Figure 5.1: Jets multiplicity in semileptonic $t\bar{t}$ events: (a) all jets; (b) jets with $p_T > 25\,\text{GeV}$

In this analysis exactly four jets with $p_T \geq 25\,\text{GeV}$ have to be reconstructed per event, with at least three of those satisfying $p_T \geq 30\,\text{GeV}$ and at least one with $p_T \geq 40\,\text{GeV}$. Inspite of the strict cut on the number of jets and on the transverse momenta, the majority of $t\bar{t}$ events with exactly four high-p_T jets pass the cut as the jet transverse momenta lie above the thresholds in most cases (see Figure 5.2). The physical background is most effectively reduced through the p_T-cut on the third and forth leading jet.

Events with more jets are discarded because it is significantly harder to assign the correct jets to the W boson and top quark for these, which greatly increases the combinatorial background (see Section 5.2).

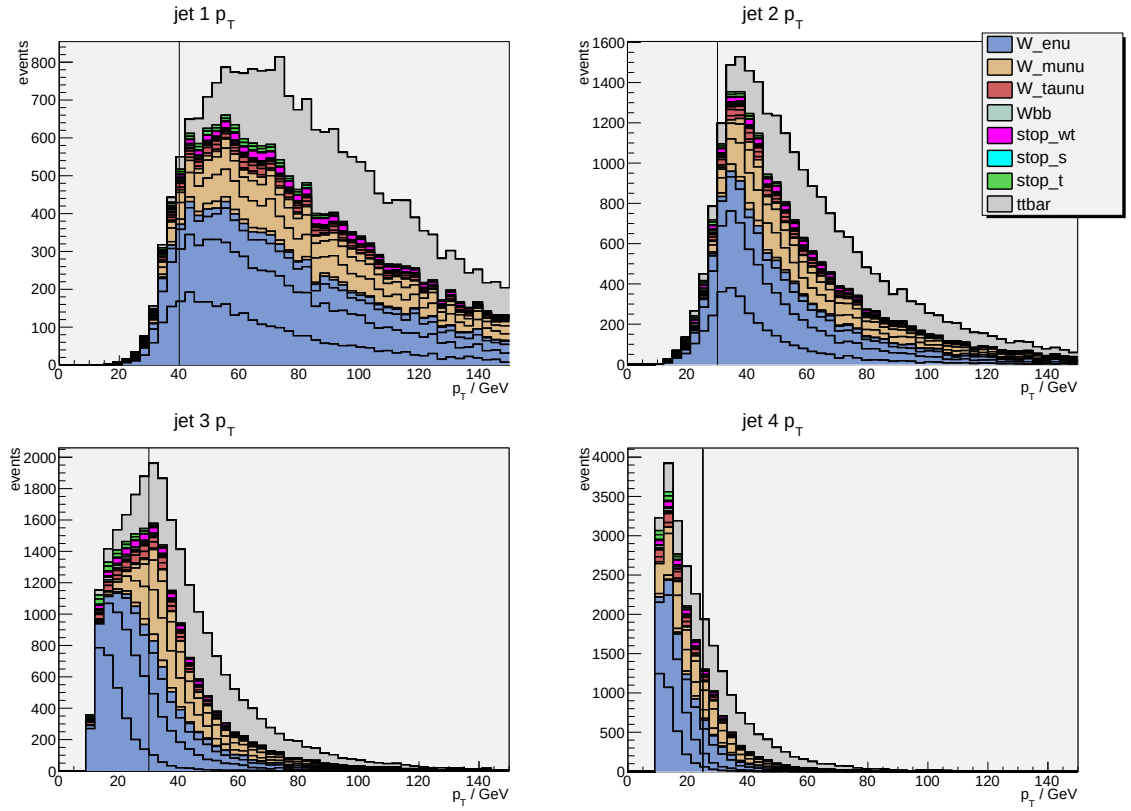

Figure 5.2: Transverse momentum of the four leading jets before cuts for signal and background

In addition, exactly one isolated high-p_T electron or muon is required, with a transverse momentum of at least 20 GeV and no jet within a cone of $\Delta R = 0.4$ around the lepton, to exclude leptons arising from weak decays in the parton shower.

For both leptons and jets only objects with $|\eta| < 2.5$ are taken into account. A cut on $\not{E}_T \geq 20$ GeV and requirements on b-tags are very useful for background reduction but are omitted for the scenario for early data (see Section 4.1.5).

5.1.2 Signal Efficiency and Background Suppression

Table 5.1 shows the cut efficiencies of the preselection cuts for the signal and background samples.

Sample	N events	After lepton cut	After jet p_T cuts
semileptonic $t\bar{t}$	11885	6958	2110
$W \rightarrow e + \nu$ + Jets	37800	20483	869
$W \rightarrow \mu + \nu$ + Jets	11930	6160	943
$W \rightarrow \tau + \nu$ + Jets	22000	1561	183
$W + b\bar{b}$ + Jets	1790	642	38
single top (s chan.)	120	66	2
single top (t chan.)	3430	1416	21
single top (wt chan.)	1430	639	82

Table 5.1: The number of events (scaled to 100 pb^{-1}) in the signal and background samples before and after the preselection cuts

The cuts effectively discriminate the background against the signal, but a significant part of the W + Jets background survives them. The single top quark production processes are well suppressed, as are all other physics processes like $W + b\bar{b}$ + associated jets.

5.2 Signal and Combinatorial Background

Once the signal is separated from the background the three out of the four high-p_T-jets originating from the hadronic top decay have to be determined. Within such a triple two jets have to be assigned to the hadronic W decay, and one to the b quark. The remaining fourth jet is considered to be the other b quark jet from the leptonic part of the decay. Wrong jet assignments are called *combinatorial background*, whereas the events with correctly assigned jets are labelled *signal* in the following.

The *truth information* contained in the Monte Carlo samples, describing the top pair decay products in their final state as Lorentz vectors, can be used to determine if the jets have been assigned to the right particles. For this purpose the geometrical distance $\Delta R = \sqrt{\Delta\Phi^2 + \Delta\eta^2}$ between the Lorentz vectors of the reconstructed jet and the final state parton in the truth information is calculated, and values below 0.4 are considered a match.

With four jets passing the preselection cuts, there are six possible 2-jet combinations that can be assigned to the hadronically decaying W boson (because the two jets are interchangeable), and two more possibilities to assign one of the remaining jets to the hadronic b quark. That gives a total of 12 possible top quark reconstructions, of which only one is correct (labelled “correct

assignment" in Table 5.2). If events with five jets were allowed in the preselection cuts, the number of reconstrucions would even increase to 60 for those.

It should be noted that incorrect reconstructions can carry information, too: an event with only correctly assigned W jets ("correct W jets, wrong top" in Table 5.2) is still perfectly useable for the determination of the W boson mass, and an event with the right three jets assigned to the partons from the top quark, but a wrong one for the b quark from the hadronic top decay ("correct top, wrong W jets" in Table 5.2) gives the correct top mass but a wrong W mass.

Reconstructions in which the b quark jet from the leptonic top quark decay is assigned to a W-jet form the rest of the combinatorial background ("other combinatorial background" in Table 5.2).

In addition to the wrong jet assignments described above, there is the possibility that a jet originating from initial or final state radiation passes the preselection cuts rather than a jet from the top pair decay. This can happen if that jet is emitted very centrally in the detector and, as a consequence, has a high transverse momentum. Another complication is that jets might alter their direction significantly if a high momentum transfer occurs through final state radiation – that can lead to a reconstructed jet with a geometrical distance to the Lorentz vector of its corresponding truth particle of $\Delta R > 0.4$, and the reconstruction is considered wrong even if it is, in fact, correct.

Both these phenomena are indistinguishable in the analysis, and together amass to more than half of the events ("not matchable" in Table 5.2) that pass the preselection cuts: Of the 2110 $t\bar{t}$ events only for 962 a reconstruction can be found that matches the truth information.

With 12 possible reconstructions per event, there are a total of 25320 reconstructions. The results of a comparision of those with the truth information from the Monte Carlo samples are given in Table 5.2.

Reconstruction	N events (after cuts)	% of total
correct assignment (W and top)	962	3.8%
correct W jets, wrong top	1318	5.2%
correct top, wrong W jets	3349	13.2%
other combinatorial background	4309	17.0%
not matchable	15382	60.8%

Table 5.2: Total number of possible reconstructions of the $t\bar{t}$ events (for 100 pb^{-1})

If the preselection requires one b-tag, the number of possible reconstructions is halved to six. With two b-tags, only two possibilities to assign the jets remain. Hence b-tagging will greatly simplify this step and remove a large part of the combinatorial background once it is usable.

5.3 Top Quark Reconstruction using Geometric and Kinetic Criteria

A strategy is needed to find the correct assignment for an event with high probability. The aim is to achieve a good background reduction while maintaining a high signal efficiency. The conventional methods for top pair decays in the semileptonic channel, described in this section, use geometic or kinetic characteristics of the jets to reconstruct the event.

5.3.1 Geometric Distance Minimisation

In the reference frame of the $t\bar{t}$ system the top and antitop quark are emitted back to back, i.e. into opposite directions. In the hadronic decay the two jets originating from the light quarks are, on average, closer to each other (in terms of ΔR) than to the hadronic b quark jet. Even though the pair is heavily boosted due to the high collision energy this fact allows for a jet assignment based on the geometric properties of the event.

The geometric criterion translates directly into the value of ΔR. The 2-jet combination with the smallest value of ΔR is assumed to be the light quark jets from the hadronic W decay; the jet of the remaining two that is closer to the vector sum of the light quark jets (i.e. the W boson) is likely to be the b quark jet from the hadronic top decay. For the efficiencies achieved see Table 5.3.

Reconstruction	N events (after cuts)	% of total
correct assignment (W and top)	223	10.6%
correct W jets, wrong top	217	10.3%
correct top, wrong W jets	443	21.0%
other combinatorial background	406	19.2%
not matchable	821	38.9%

Table 5.3: Signal and combinatorial background after event reconstruction (ΔR mimimisation)

5.3.2 Transverse Momentum Maximisation

A different but similar approach in terms of physics is to consider the two jets with the highest combined p_T (i.e. the transverse momentum of the vector sum) as the W boson and then select the remaining jet that maximises the 3-jet transverse momentum as the hadronic b quark jet. The selection efficiencies achieved with this method are listed in Table 5.4.

Reconstruction	N events (after cuts)	% of total
correct assignment (W and top)	167	7.9%
correct W jets, wrong top	209	9.9%
correct top, wrong W jets	476	22.6%
other combinatorial background	429	20.3%
not matchable	829	39.3%

Table 5.4: Signal and combinatorial background after event reconstruction (2-jet (W) p_T maximised first, then 3-jet (top) p_T)

Alternatively it is possible to first choose the three jets with the highest combined p_T as the hadronically decaying (anti-)top quark and afterwards distinguish between light quark jets and the b quark jet by looking for the 2-jet combination with the highest p_T within those three jets. The results are very similar to those from the method above, see Table 5.5.

A combination of ΔR minimisation and p_T maximisation is possible but does not lead to better selection efficiencies; ΔR minimisation yields the best result. The overall signal selection efficiency (i.e. purity times efficiency) for this method is 1.8%.

Reconstruction	N events (after cuts)	% of total
correct assignment (W and top)	169	8.0%
correct W jets, wrong top	211	10.0%
correct top, wrong W jets	486	23.0%
other combinatorial background	413	19.6%
not matchable	831	39.4%

Table 5.5: Signal and combinatorial background after event reconstruction (3-jet (top) p_T maximised first, then 2-jet (W) p_T)

5.3.3 Cuts

After reconstruction, the signal purity is increased by the application of appropriate cuts. Standard cuts include a mass window for the W boson ($80.4\,\text{GeV} \pm 2 \cdot \sigma_\text{W}, \sigma_\text{W} = 10.4,\text{GeV}$ [32]) and a cut on the invariant mass of the hadronic W boson and the leptonic b quark jet ($> 200\,\text{GeV}$) [33]. The overall signal efficiency and purity for these cuts is shown in Table 5.6.

Cut/Reconstruction	Efficiency	W purity	top purity	top+W purity
preselection	17.73%			
reconstruction (min. ΔR)	17.73%	20.9%	31.6%	10.6%
cut: W mass	8.47%	33.4%	40.6%	19.0%
cut: W + leptonic b invariant mass	5.92%	33.9%	47.9%	25.2%

Table 5.6: Signal efficiency and purity for the reconstruction

5.4 Top Quark Reconstruction using a Multivariate Analysis

A multivarate analysis can be used to separate the combinatorial background from the signal. For this purpose all possible *reconstruction candidates*, i.e. the twelve possible assignment combinations of the four high p_T jets to form the hadronic W boson and the hadronic top quark, are evaluated by a classifier, which returns a score determining how "signal-like" the candidate is. Thus, instead of choosing the appropriate reconstruction based on a single geometric criterion, several aspects of the kinematics of the top pair decay can be taken into account.

Instead of cutting on specific values for kinematic variables after the reconstruction to increase the signal purity, these variables can be used as an input for the classifier and in that way influence the decision on which reconstruction to select. The result is a higher signal efficiency with a comparable purity.

5.4.1 Machine Learning and Classifiers

Classifiers are algorithms from the field of machine learning, a research area dealing with the automatic recognition of patterns and rules in data [34]. They attempt to classify an input object as belonging to a certain predefined category. In experimental particle physics the usual set of categories, used to classify events in a detector, only consists of *signal* and *background*.

The methods introduced here are a form of supervised learning, where the patterns are deduced from a set of training data. With this information the algorithms are trained, and from the patterns recognised further events can be classified.

The events are described with a set of variables. These have to be relevant criteria in the distinction between signal and background, and relatively few variables should be chosen for this purpose. With a bigger set of input values the required amount of training data increases, and so does the likelihood of overfitting.

Different classifiers achieve their common goal through different strategies [35]:

- Boosted Decision Trees (BDT) generate a set of decision trees from the training data,
- Artificial Neural Networks (ANN) form a multi-layered set of artificial neurons and connections between them,
- the K Nearest Neighbours algorithm (KNN) determines the class of the object from the classifications of its nearest neighbours in the multi-dimensional phase space,
- Support Vector Machines (SVM) construct a hyperplane in the phase space that maximises the margin between signal and background in that space, and classifies new events according to their position regarding that hyperplane using a linear or polynomial kernel.

Many more algorithms exist. The big advantage in the use of automated classification is that correlations of the input variables can be taken into account, which is not the case in a cut-based analysis.

The performance of classifiers is evaluated through cross-checks with more objects for which the real category is known. For the purpose of distinguishing signal from background events the most relevant criteria are signal efficiency and background reduction.

5.4.2 The Toolkit for Multivariate Data Analysis

TMVA, the Toolkit for Multivariate Data Analysis [36], is a package for the ROOT analysis framework that provides training, testing, and evaluation for several multivariate classifiers including KNN, BDT, MLP ANN and SVM. It is designed for, but not limited to, the use in high energy physics. This analysis relies on the classifier implementations of TMVA.

5.4.3 Input Variables and Classifier Training

The input variables, or discrimination variables, used to train the classifiers and to evaluate the events are supposed to replace the geometric criteria for the event reconstruction as well as the post-selection cuts normally used to suppress the combinatorial background. All possible combinations of jet associations are formed and classified by TMVA. For the training stage the reconstructions of a random subset of events from the Monte Carlo sample are used. The true class (signal or combinatorial background) of those possible reconstructions is determined from the Monte Carlo truth information as described in Section 5.2.

Naturally the input variables are similar to those used in the reconstruction and for cuts:

- The W boson mass,
- the geometric distance ΔR between the light quark jets,
- the transverse momentum of the hadronic b quark jet in the 3-jet centre-of-mass frame,
- the balance of the energies of the W boson and b quark in the 3-jet centre-of-mass frame and
- the ratio of the momentum over the mass of the top quark in the 3-jet centre-of-mass frame.

The normalised distributions for signal and background for these variables is shown in Figure 5.3.

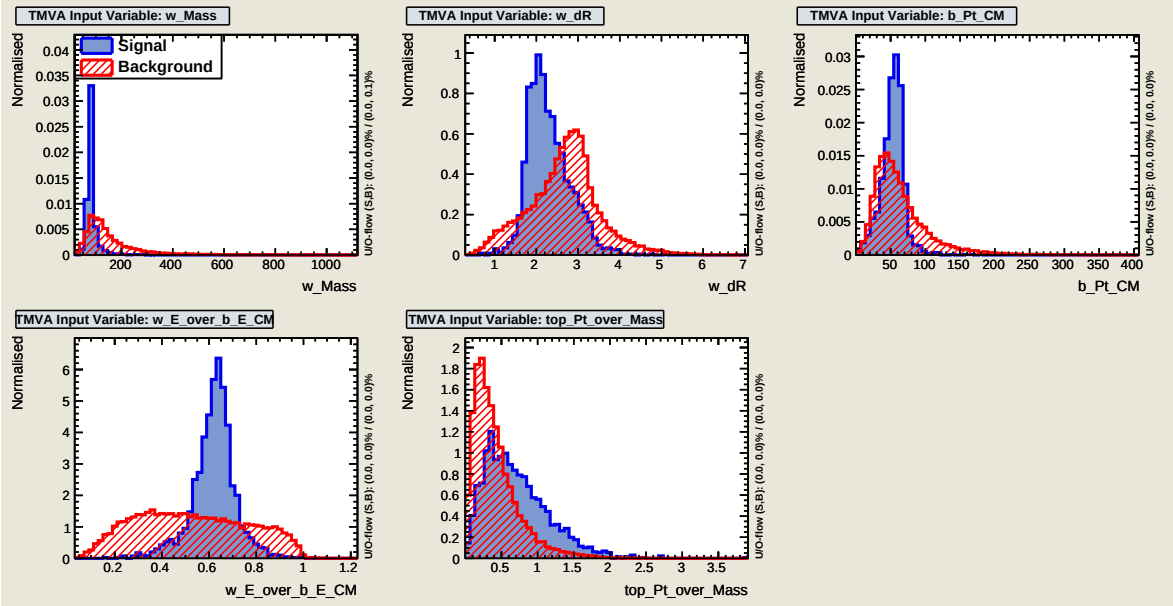

Figure 5.3: The input variables for TMVA with their distributions for signal and background

The first variable (*w_Mass* in Figure 5.3), the 2-jet mass of light quark jets from the hadronic W decay, obviously peaks at the well known W mass if the right jets are selected. This replaces the cut on the W mass.

Similar to the geometric reconstruction is the second variable (*w_dR* in Figure 5.3): The geometric distance between the two light quark jets is smaller on average for the correct assignment.

Next, the two input variables that describe energies and momenta in the 3-jet centre-of-mass frame are kinetic property of the two body decay of the top quark in its rest frame. With a top quark mass of roughly 170 GeV, a W mass of 80.4 GeV and a much lower b quark mass, and the b quark and the W boson emitted back to back, the transverse momentum of the b quark (*b_Pt_CM* in Figure 5.3) peaks at ≈ 80 GeV. Additionally, from energy conservation

$$E_{\text{top}} = E_{\text{W}} + E_{\text{b}}$$

$$E_{\text{top}}^2 = E_{\text{W}}^2 + E_{\text{b}}^2 + 2E_{\text{W}}E_{\text{b}}$$

follows, using the relativistic energy (in natural units where $c = 1$)

$$E^2 = m^2 + \boldsymbol{p}^2$$

where m is the rest mass of the particle, and p its momentum:

$$m_{\text{top}}^2 + \boldsymbol{p}_{\text{top}}^2 = m_{\text{W}}^2 + m_{\text{b}}^2 + \boldsymbol{p}_{\text{W}}^2 + \boldsymbol{p}_b^2 + 2E_{\text{W}} \cdot (E_{\text{top}} - E_{\text{W}})$$

Using momentum conservation, $\boldsymbol{p}_{\text{W}} = -\boldsymbol{p}_b$, and the fact that the calculation is done in the rest frame of the top quark ($\boldsymbol{p}_{\text{top}} = 0$, $E_{\text{top}} = m_{\text{top}}$) gives

$$m_{\text{top}}^2 = m_{\text{b}}^2 - m_{\text{W}}^2 + 2E_{\text{W}} \cdot m_{\text{top}}$$

$$E_{\text{W}} = \frac{m_{\text{top}}^2 + m_{\text{W}}^2 - m_{\text{b}}^2}{2m_{\text{top}}}$$

and similarly

$$E_B = \frac{m_{\text{top}}^2 + m_{\text{b}}^2 - m_{\text{W}}^2}{2m_{\text{top}}}$$

Here the term m_{b}^2 can be neglected as it is small, and for the ratio of the energies of the decay products we have

$$\frac{E_{\text{b}}}{E_{\text{W}}} \approx \frac{m_{\text{top}}^2 - m_{\text{W}}^2}{m_{\text{top}}^2 + m_{\text{W}}^2}$$

which gives a value between 0.6 and 0.7 for values of m_{top} between 160 GeV and 190 GeV and $m_{\text{W}} =$ 80.4 GeV. The energies and momenta in the 3-jet centre-of-mass frame are obtained through a Lorentz re-boost, with the vector sum of the Lorentz vectors of the three jets used as the boost vector, with opposite sign.

The last variable (*top_Pt_over_Mass* in Figure 5.3) is a replacement for the maximum-p_T criterion. While the absolute value of the top quark transverse momentum is not useful because the $\text{t}\bar{\text{t}}$ pair is heavily boosted with respect to the laboratory frame, it gains separation power when divided by the 3-jet mass: The correct combinations tend to have a higher value for this ratio. This is a similar statement to the one that the 3-jet combination with the highest combined p_T is likely to be the correct reconstruction, but expressed in a continuous variable that allows a better evaluation by TMVA.

5.4.4 Classifier Performance and Output

Using the same events for both training and testing would lead to overly optimistic assumptions for the achieved level of signal efficiency and background suppression, a phenomenon called *overtraining* or *overfitting*. To avoid this, a subset of the available events is not used to train but to test the classifier response in order to assess the performance of the various classifiers.

The signal efficiencies achieved by the multivariate classifiers are plotted against the corresponding background rejection in Figure 5.4.

The more sophisticated classifiers like the artificial neural network or Boosted Decision Trees perform better than simpler ones like Fisher discriminants, which can be seen in their superior background suppression for the same signal efficiency in Figure 5.4. The fact that a similar performance can be achieved by a whole group of different classifiers indicates that the algorithms do

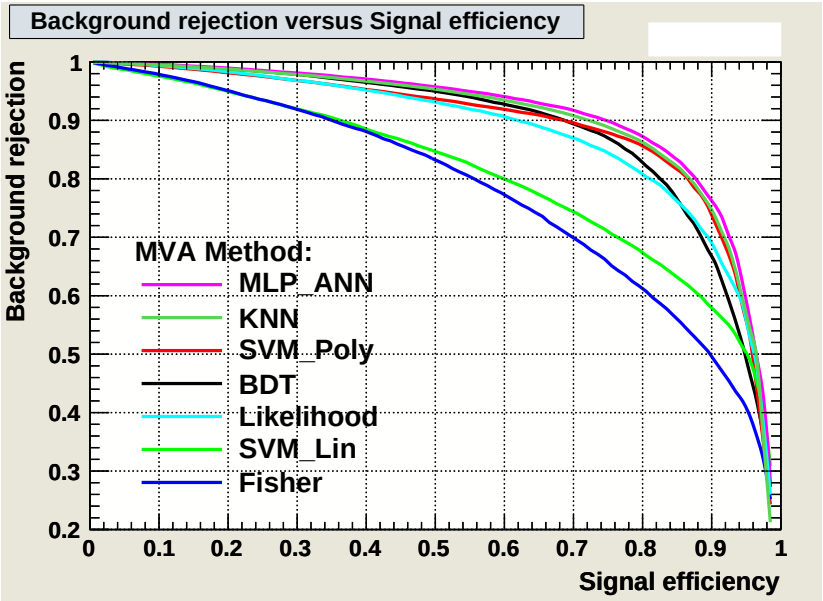

Figure 5.4: Background rejection plotted against signal efficiency for different TMVA classifiers

not suffer heavily from overtraining and that the predicted level of background reduction and signal efficiency can actually be reached using real data as well.

The artificial neural network (MLP_ANN) yields the best results among the tested classifiers and is used throughout the analysis. Its performance is shown in Figure 5.5. However, the achieved maximum significance (the peak value of the green curve) is not the only important property of the classifier: The signal efficiency (solid blue line) must not change drastically with the output value because the performance should remain predictable when the kinematics of the events change slightly, e.g. through a variation of the top quark mass or the Jet Energy Scale, which generally leads to lower output values for signal events; the same holds for the level of backgrond suppression (red curve). The MLP ANN classifier fulfills this requirement.

The signal purity is shown as the upper dashed blue curve in Figure 5.5. A high purity is desireable, but the product of purity and efficiency (lower dashed blue curve) is a better measure to assess the classifier performance because the number of signal events that pass the analysis (i.e. the efficiency times number of events available for analysis) determines the statistical uncertainty. Purity times efficiency is correlated with the significance.

Figure 5.5 is to be interpreted in terms of a *cut off value*, i.e. a minimum output value of the classifier. Only event reconstructions that return a higher score are kept. If the cut off is set at 0.0, the signal efficiency is 50%, background reduction ca. 93% and signal purity ca. 40%. Signal purity times efficiency is, consequently, at 20%, and the significance at value of 20.

A higher cut off value would, for example, increase the signal purity but reduce the signal efficiency, leading to a lower significance. A lower cut off value would in turn improve the signal efficiency at the cost of a lower background reduction. A compromise has to be found that best fits the needs of the analysis. Note that all these values are dependent on the individual training and have to be evaluated separately for different classifiers and different training data sets.

Choosing the cut off value replaces optimising the post-selection cuts described in Section 5.3.3 but is somewhat more convenient as a desired signal efficiency or purity can be achieved simply

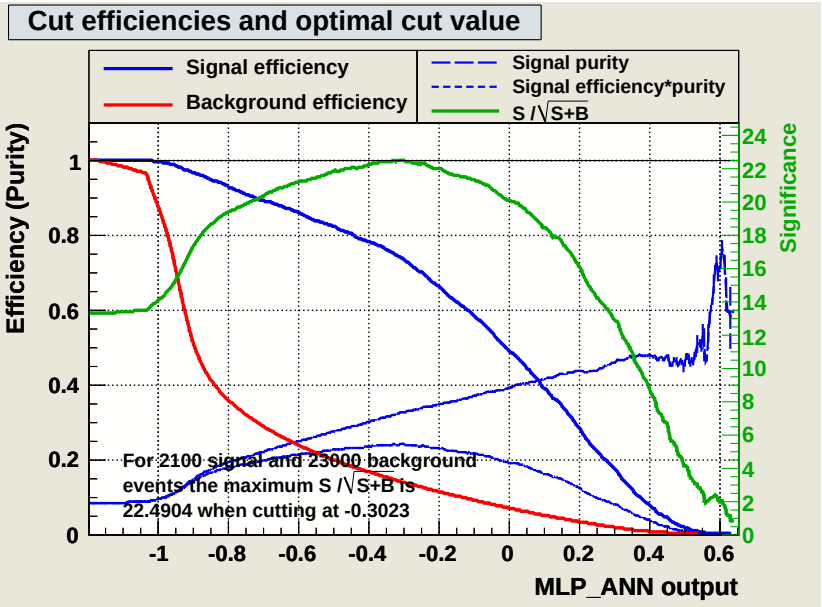

Figure 5.5: Background rejection, signal efficiency and significance plotted against the classifier output value for the MLP ANN classifier

by requiring the classifier output to be above this threshold. For the analysis the cut off value has been set to −0.3.

5.4.5 Event Weighting and Selection Efficiencies

The fact that the classifier returns a numeric value allows for two different strategies to weight the candidates according to this score.

The first (and simpler) strategy is to take from every event the reconstruction that yields the highest score, if that score is above the cut off threshold. That gives the most likely reconstruction and discards events where no good reconstruction is possible, e.g. physical background and $t\bar{t}$ events where the wrong jets passed the pre-selection cuts (but some signal events, too). The results are listed in Tables 5.7 and 5.8.

Reconstruction	N events (after cuts)	% of total
correct assignment (W and top)	394	25.2%
correct W jets, wrong top	58	3.7%
correct top, wrong W jets	181	11.6%
other combinatorial background	343	21.9%
not matchable	590	37.7%

Table 5.7: Signal and combinatorial background after event reconstruction with MLP ANN classification

Alternately it is possible to only reject the reconstructions with a score below the cut off value and weight the remaining ones according to their score, which allows several different reconstructions per event to contribute to the analysis, smoothening the distributions for the 2-jet and 3-jet masses. The weights should be normalised so that all the weights from passing event reconstruc-

Cut/Reconstruction	Overall efficiency	W boson purity	top purity
preselection	17.73%		
TMVA reconstruction	13.16%	28.9%	36.8%

Table 5.8: Signal efficiency and purity for the reconstruction

tions from a single event add up to a total of one. However, as the classifier score is not a probability, the weighting is arbitrary and non-linear, and the systematic errors caused by this are difficult to estimate.

Tables 5.9 and 5.10 show the efficiencies and purities for the signal and combinatorial background with this reconstruction method. They are inferior to the ones achieved with the simple selection of the reconstruction (cf. Tables 5.7 and 5.8), which is thus used for the further analysis.

Reconstruction	N events (after cuts)	% of total
correct assignment (W and top)	363	22.1%
correct W jets, wrong top	52	3.2%
correct top, wrong W jets	194	11.8%
other combinatorial background	367	22.3%
not matchable	668	40.6%

Table 5.9: Signal and combinatorial background after event reconstruction with MLP ANN classification, event weights from classifier output

Cut/Reconstruction	Overall efficiency	W boson purity	top purity
preselection	17.73%		
TMVA reconstruction	13.82%	25.2%	33.9%

Table 5.10: Signal efficiency and purity for the reconstruction, event weights from classifier output

5.4.6 Physical Background Reduction

Through the cut-off value in the multivariate analysis a part of the physical background is suppressed. Table 5.11 shows the number of remaining events per sample that have a reconstruction with a score above the threshold.

The physical background is reduced more strongly than the $t\bar{t}$ sample, which is desirable. A second, independent set of cuts or multivariate classification might improve the background reduction further.

5.5 Comparison of the Methods

The significance, defined as

$$S = \frac{N_S}{\sqrt{N_S + N_B}}$$

Sample	N events	Preselection	TMVA
semileptonic $t\bar{t}$	11885	2110	1566
$W \rightarrow e + \nu$ + Jets	37800	869	528
$W \rightarrow \mu + \nu$ + Jets	11930	943	559
$W \rightarrow \tau + \nu$ + Jets	22000	183	80
$W + b\bar{b}$ + Jets	1790	38	24
single top (s chan.)	120	2	1
single top (t chan.)	3430	21	8
single top (wt chan.)	1430	82	65

Table 5.11: The number of events (scaled to 100 pb^{-1}) in the signal and background samples before and after the reconstruction and the cuts

where N_S is the number of signal events and N_B the number of background left events after the reconstruction and cuts, is a measure of quality of the data used for the mass measurement. To evaluate the different techniques used for the event reconstruction only combinatorial background is considered here.

Signal is an ambiguous term here: For a measurement of the 3-jet mass of the hadronic top, it is sufficient that the correct three jets have been assigned to the top quark, and the jets from the hadronic W and b can be interchanged. The significance for this definition is labelled S_t. In contrast, S_{t+W} is used to describe the reconstructions where the jets have not only been correctly assigned to the top quark, but to its decay products as well.

Reconstruction	S_t	S_{t+W}
min. ΔR	17.55	5.15
+ Cut: W mass	16.72	6.70
+ Cut: W + leptonic b invariant mass	17.61	7.73
TMVA (MLP ANN)	16.91	10.15

Table 5.12: The significance achieved with the different methods for the event reconstruction

As can be seen in Table 5.12, the TMVA analysis has a comparable significance to the geometric reconstruction if S_t is used as a guideline. In contrast, if the focus lies on events where the jets from the top quark decay have been assigned to the W boson and b quark correctly, the multivariate analysis improves the result by over 30%.

This analysis relies on both a reconstruction of the top quark and the W boson, which makes a high value for S_{t+W} desirable. As a consequence, the multivariate analysis is used for the measurement presented in the next chapter.

Chapter 6

Determination of the Top Quark Mass

After the events have been reconstructed the calculation of the top quark mass can be performed. This is done for several different simulated top quark masses in this chapter. For an analysis of early data a method is presented to determine the top mass even with a high uncertainty on the Jet Energy Scale. An integrated luminosity of $\int \mathscr{L}\,\mathrm{dt} = 100\,\mathrm{pb}^{-1}$ is assumed, and all diagrams in this chapter are scaled appropriately and the statistical error limits are given in accordance.

6.1 The 3-Jet Invariant Mass

The invariant mass of the top quark is calculated relativistically from the energies E_i and momenta $\boldsymbol{p}_i$ of the three jets originating from its decay, which are measured in the hadronic calorimeter of the ATLAS detector:

$$m_{\mathrm{top}} = m_{3-\mathrm{jet}} = \sqrt{\left(\sum_{i=1}^{3} E_i\right)^2 - \left(\sum_{i=1}^{3} \boldsymbol{p}_i\right)^2}$$

The invariant mass of the W boson is determined in a similar manner by taking the two light quark jets into account only.

The left diagram in Figure 6.1 shows the distribution of the 3-jet mass, with the reconstruction done using the multivariate analysis with TMVA, for the Monte Carlo sample with $m_{\mathrm{top}} = 172.5\,\mathrm{GeV}$, including all relevant background processes except for QCD multijet production. The red area describes the events for which the hadronic top quark and W boson were reconstructed correctly; green, blue, yellow and grey are the various types of combinatorial background as explained in Section 5.2. The region below (pink, brown, blue) represent the physical background from single top production and the W + Jets processes.

On the right side in Figure 6.1 a fit function is plotted that approximates the distribution. For the physical and combinatorial background a superposition of two Landau curves is used (brown and grey curves), and the signal is modelled with a Gaussian (red curve). The fit is not perfect: the physical background is slightly overestimated, especially in the bins that represent a low 3-jet mass, and the signal peak is slightly shifted towards lower masses. However, the sum of the two Landau curves approximates the sum of physical and combinatorial background well, and this

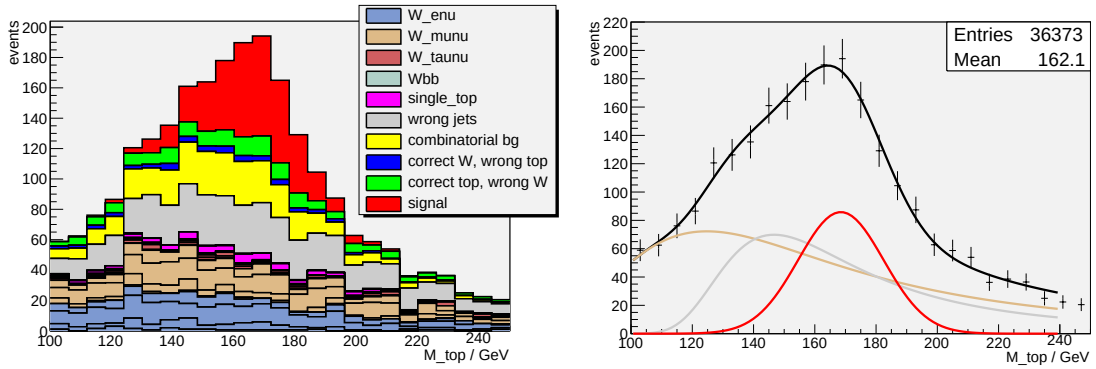

Figure 6.1: The 3-jet mass for the central mass point, including physical and combinatorial background (left) and the fit function to approximate the distribution (right)

model is useful as it uses relatively few parameters (three per curve) and can be used over a wide range of top mass points and JES deviations.

When fitted with this set of functions, the 3-jet mass peak is located at

$$m_{3-\text{jet}} = 168.5\,\text{GeV} \pm 2.5\,\text{GeV(stat.)}$$

with the error stemming from the statistical uncertainties that limit the precision of the fit function. The error bars in the right diagram in Figure 6.1 represent those statistical uncertainties, i.e. the square root of the number of events in each bin as expected for $100\,\text{pb}^{-1}$. The fact that the 3-jet mass is below the simulated top quark mass, even considering the error limits, can be attributed to final state radiation and its lowering effect on the jet energies, and to systematic effects of the event selection process.

All fits are performed with the MINUIT [37] package for the ROOT framework [24], using a χ^2-minimisation.

6.2 Variation of the Simulated Top Mass

The Monte Carlo samples for the semileptonic $t\bar{t}$ decay, listed in Section 4.4.1, are used to test the ability of the analysis to reconstruct different top quark masses. This is important to verify that the classifier does not only select events and reconstructions with the 3-jet mass used for training (172.5 GeV) but is actually useful for a mass measurement.

The 3-jet mass distributions for $m_{\text{top}} = 160\,\text{GeV}$ and $m_{\text{top}} = 180\,\text{GeV}$ are shown in Figure 6.2. The larger statistical fluctuations arise from a smaller Monte Carlo sample size, and for the higher simulated top quark mass from the lower $t\bar{t}$ production cross section.

Evidently the combinatorial background, especially the grey and yellow areas, changes its shape and peak value only slightly with an alternating top mass. That suggests that it does not contain relevant information about the top quark mass and should be treated separately from the signal region, e.g. with a separate Landau curve in the fit to approximate the data as described in Section 6.1. The reconstructed 3-jet masses for the different top – anti-top samples is thus only obtained from the peak of the Gauss part of the fit function; the results for the different simulated mass points are listed in Table 6.1 with their statistical errors as determined by the fit algorithm. Once

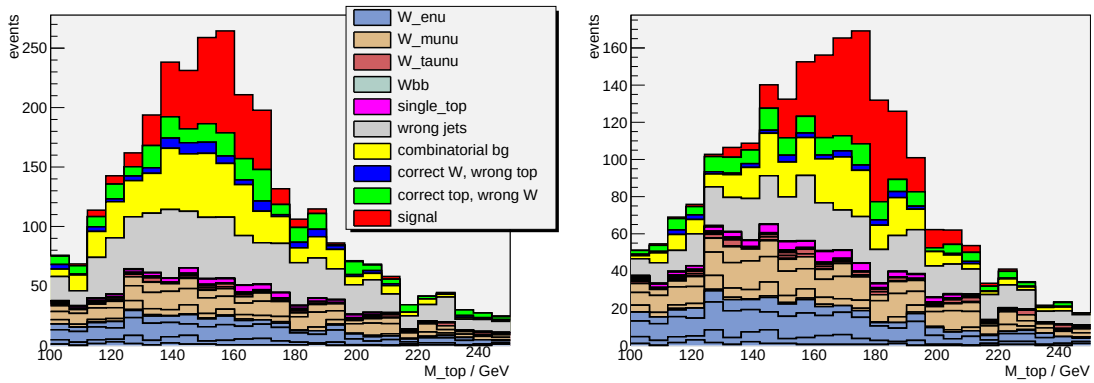

Figure 6.2: The 3-jet mass for simulated top quark masses of 160 GeV (left) and 180 GeV (right)

again the effect is visible that the measured 3-jet mass is generally lower than the simulated top quark mass.

Simulated m_{top} [GeV]	Reconstructed $m_{3-\text{jet}}$ [GeV]
160	157.5 ± 2.7
170	163.3 ± 3.1
172.5	168.4 ± 2.5
180	173.1 ± 2.8
190	181.9 ± 2.1

Table 6.1: Simulated and reconstructed top quark masses (with statistical errors) for the different $\text{t}\bar{\text{t}}$ Monte Carlo samples

It should be noted that not only the $\text{t}\bar{\text{t}}$ production cross section changes with m_{top}, but also the event kinematics. As a consequence the number of events available for analysis and the signal efficiency of the classifier are different for the alternating simulated mass points. The data listed in Table 6.2 shows that while the cross section is higher for lower values for the top mass, the efficiency of the cuts and the reconstruction is inferior to that for the central mass point. Towards higher top quark masses the lower cross section and resulting low number of events becomes increasingly problematic, leading to higher statistical errors. For low masses, in particular for the $m_{\text{top}} = 160\,\text{GeV}$ sample, the selection efficiency decreases because the jets have lower transverse momenta, meaning that fewer events pass the preselection cuts. Additionally some kinematic properties, e.g. the energy balance, differ from the events used to train the classifier, which leads to a lower efficiency of the artificial neural network used to choose the jet assignments.

6.3 3-Jet to 2-Jet Mass Ratio

The precision of the 3-jet mass measurement presented in Sections 6.1 and 6.2 depends heavily on the Jet Energy Scale (see Section 4.1.3). Its systematic errors will probably be the biggest source of uncertainty on the top quark mass in an analysis with early data.

The fact that the mass of the W boson is well known through various measurements at different experiments – it is currently given by the Particle Data Group (PDG) as $m_{\text{W,PDG}} = 80.398 \pm 0.025\,\text{GeV}$

Simulated m_{top}	N events	N events after preselection	N_S after reconstruction
160 GeV	17000	2950	441
170 GeV	12700	2329	441
172.5 GeV	11900	2110	394
180 GeV	9600	1850	369
190 GeV	7300	1432	247

Table 6.2: Number of events for the different $t\bar{t}$ samples; N_S is the number of signal (i.e. correctly reconstructed) events

[2] – is a chance to work around the uncertainties on the JES. This mass can be used to calibrate the top quark mass measurement by calculating

$$m_{\text{top}} = \frac{m_{3-\text{jet}}}{m_{2-\text{jet}}} \cdot m_{\text{W,PDG}}$$

instead of just using $m_{\text{top}} = m_{3-\text{jet}}$. $m_{2-\text{jet}}$ is the measured invariant mass of the reconstructed hadronic W boson, calculated from the energies and momenta of the two light quark jets from the W decay. Because those jets are also included in the computation of $m_{3-\text{jet}}$, uncertainties in their measurement cancel out. The calculation can either be performed on a single event basis, or for the peaks of the summed up distributions of all events.

Several different aspects of the Jet Energy Scale have to be considered: Random, statistical deviations due to a limited resolution, systematic scaling, and an additional correction factor for b quark jets. The statistical deviations are dealt with using a high number of events, but this method provides a chance to cancel out the errors when used per event; a linear scaling of the JES, possibly from final state radiation, should cancel out completely; the correction factor for b-quark jets cannot be determined or cancelled out with this calculation.

6.3.1 Event-By-Event Rescaling

The first way to implement the calibration of the top mass measurement with the W boson mass from the PDG is to perform it on a per event basis: The ratio of the 3-jet and 2-jet masses is multiplied by $m_{\text{W,PDG}}$ for every single event, and the resulting histogram can be directly evaluated to find the top mass.

With this procedure statistical fluctuations in the light quark jet energy measurement cancel out to a certain degree for the individual events as the mass of the W boson is part of the calculated top quark mass. That leads to a higher precision when so few data are available that the individual events have to be evaluated rather than their statistical distributions.

However, this approach has a big drawback when used with the event reconstruction and selection described in Section 5.4: The multivariate analysis focuses very much on kinetic criteria, e.g. the energy balance of the decay products, which causes the distribution of $m_{\text{top}}/m_{\text{W}}$ to peak around the same values for signal and background. This makes a fit to determine the mass very difficult, as can be seen in Figure 6.3.

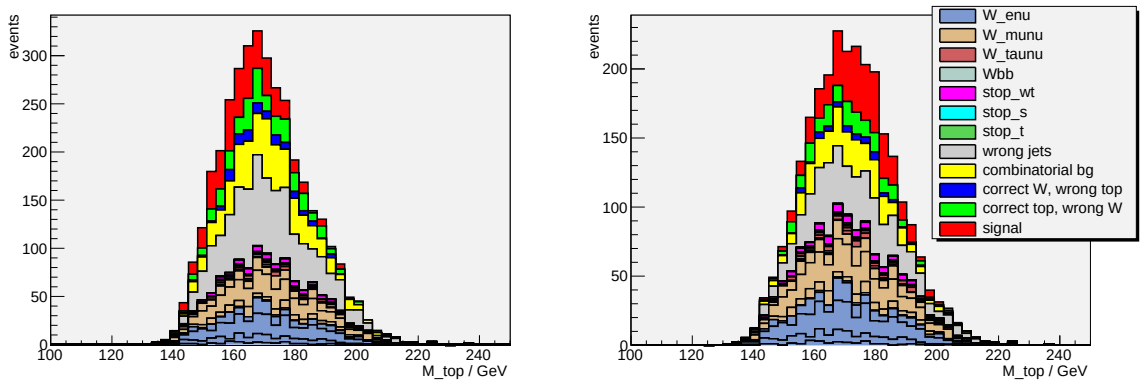

Figure 6.3: The ratio $m_{\text{top}}/m_{\text{W}}$, multiplied with $m_{\text{W,PDG}}$, for simulated top masses of 160 GeV (left) and 180 GeV (right)

6.3.2 Re-calibrating the Top Quark Mass Peak

It is also possible to first find the peaks for the W boson and top quark masses in the histograms containing all events that passed the cuts or the TMVA evaluation. The rescaled top mass then becomes

$$m_{\text{top}} = \frac{m_{\text{top,peak}}}{m_{\text{W,peak}}} \cdot m_{\text{W,PDG}}.$$

One advantage of this approach is that the events in the combinatorial background, where the right three jets for the top quark were selected, but the wrong subset for the W boson was chosen, are still perfectly useful to determine the top mass peak; events with a correct reconstruction of the W boson only can still be used to find the W mass. With the event-by-event rescaling described in Section 6.3.1, these events broaden the top peak and have to be treated as combinatorial background.

The method requires fits for the distribution of the 3-jet mass for the top quark and the 2-jet mass for the W boson. The latter suffers from the same problem that occurred in Section 6.3.1: $m_{2-\text{jet}}$ for the physical and combinatorial background peaks around the W mass and is not flat (see Figure 6.4). That is an unavoidable consequence of the event selection and reconstruction where the identification of the jets that originate from W boson decay through geometric and kinetic properties plays a crucial role.

However, the peaks for the W mass are narrow, and the combinatorial background is slightly leaning towards 2-jet masses lower than 80.4 GeV regardless of the simulated top quark mass. An approximation with a superposition of a broader Gauss curve for the background and a narrower Gauss distribution for the signal approximates the data well, as shown in Figure 6.5. Here, too, the resulting values for $m_{2-\text{jet}}$ are lower than the simulated W boson masses, for the same reasons described in Section 6.1 for the 3-jet mass.

The reconstructed W boson masses are listed in Table 6.3. A dependency on the simulated top mass is visible, leading to lower reconstructed W masses for lower simulated top quark masses. This can be attributed to the event selection process which takes the energy balance in the top quark decays into account.

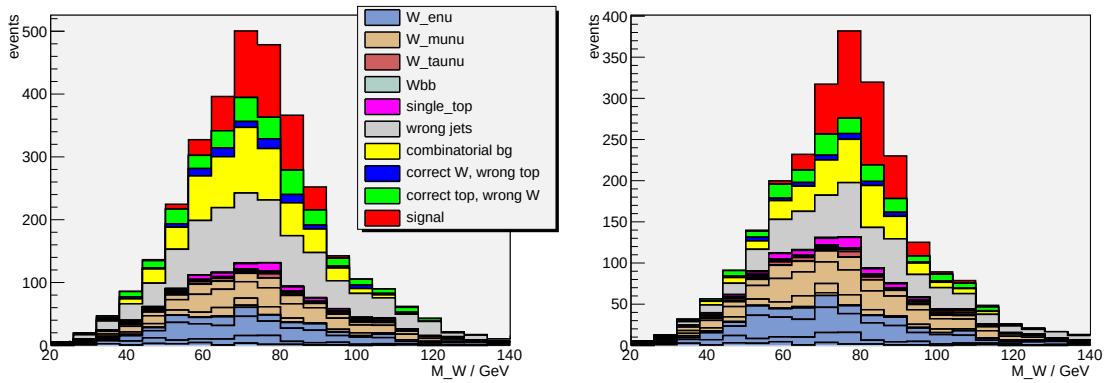

Figure 6.4: The distributions of the 2-jet mass of the reconstructed hadronic W boson, for simulated top masses of 160 GeV (left) and 180 GeV (right)

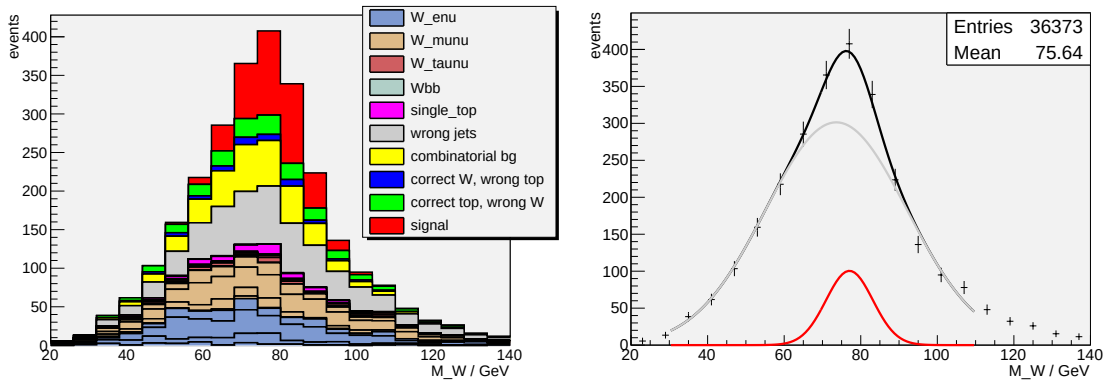

Figure 6.5: The distributions of the 2-jet mass of the reconstructed hadronic W boson, for a simulated top mass of 172.5 GeV (left); approximation with Gauss + Gauss fit (right)

6.4 Variation of the Jet Energy Scale

With an artificial scaling of the jet energies the systematic effect of a linear scaling factor on the JES can be simulated. That tests the stability of the analysis against such systematic effects, and therefore the usefulness of the calibration of the measurement with the W mass. Variations in the range between −10% and +10% are simulated in 5%-steps.

6.4.1 Impact on the Selection Efficiencies

As for the different top mass points, the selection efficiencies vary with the JES scaling. The impact is smaller than that of the top mass variation because properties like the energy balance in the event do not change significantly. With higher jet energies more events survive the preselection cut on the transverse momenta of the leading jets. The numbers of events after the preselection and reconstruction are listed in Table 6.4.

Simulated m_{top} [GeV]	Reconstructed m_{2-jet} [GeV]
160	75.3 ± 1.6
170	76.6 ± 1.1
172.5	77.1 ± 1.2
180	78.6 ± 1.1
190	78.1 ± 1.4

Table 6.3: Reconstructed W boson masses (with statistical errors) for the different $t\bar{t}$ Monte Carlo samples

JES scaling	N events	N events after preselection	N_S after reconstruction
-10%	11900	1914	364
-5%	11900	2021	382
±0%	11900	2110	394
+5%	11900	2176	403
+10%	11900	2225	398

Table 6.4: Number of events after cuts and reconstructions for the $t\bar{t}$ sample with m_{top} = 172.5 GeV with different simulated JES scaling factors; N_S is the number of signal (i.e. correctly reconstructed) events

6.4.2 Results for the 2-jet and 3-jet Masses

The effect of a linear scaling of the Jet Energy Scale on the 3-jet mass distribution is shown in Figure 6.6. Higher jet energy scales lead to broader peaks, lower energy scales to lower statistics. Even if the individual functions fail to match the combinatorial and physical background, respectively, in the low 3-jet mass region, the sum of the two Landau curves still approximates the total background well.

The five $t\bar{t}$ Monte Carlo samples are each analysed with all of the scaling factors of the JES, performing the fits on the 3-jet and 2-jet masses as described above. The results are listed in Tables 6.5 and 6.6 and plotted in Figures 6.7 and 6.8. The value on the y-axis is the reconstructed mass, the different colours represent the different top quark mass points. The error bars show the statistical uncertainties only, scaled to $\int \mathscr{L}\,dt = 100$.

Simulated m_{top} [GeV]	JES -10%	JES -5%	JES ±0	JES +5%	JES +10%
160	139.9 ± 3.5	147.6 ± 3.7	157.5 ± 2.7	162.8 ± 2.8	170.2 ± 2.5
170	148.9 ± 2.1	156.6 ± 2.9	163.3 ± 3.1	172.3 ± 2.9	178.3 ± 2.7
172.5	154.3 ± 2.2	160.9 ± 2.1	168.4 ± 2.5	176.4 ± 2.3	184.5 ± 3.5
180	158.4 ± 2.8	164.8 ± 2.4	173.1 ± 2.8	180.8 ± 2.5	189.3 ± 2.2
190	166.6 ± 2.7	174.3 ± 2.6	181.9 ± 2.1	192.0 ± 2.6	197.2 ± 2.6

Table 6.5: Reconstructed 3-jet masses (in GeV, with statistical errors) for the different $t\bar{t}$ Monte Carlo samples and JES variations

An important property of the analysis is visible in Figure 6.7: The reconstructed 3-jet mass scales linearly (within the error limits) with a variation of the Jet Energy Scale for each of the simulated top mass points, and the analysis keeps its ability to reconstruct different top masses as described in Section 6.2.

a)

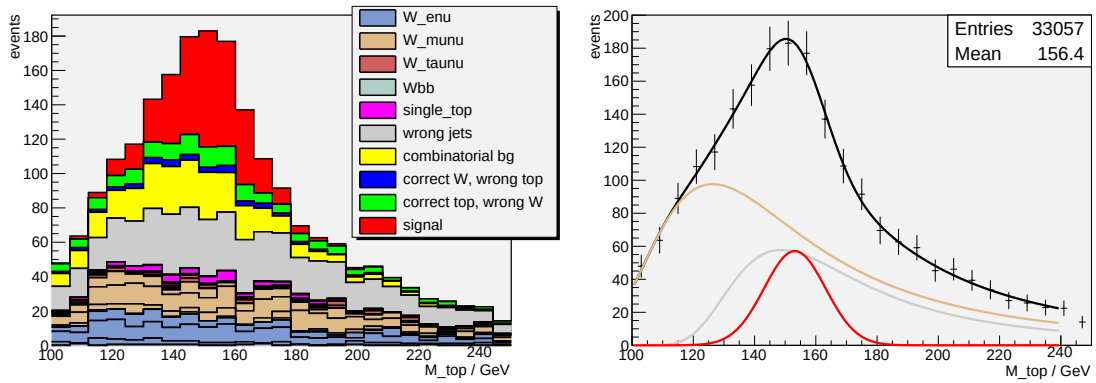

b)

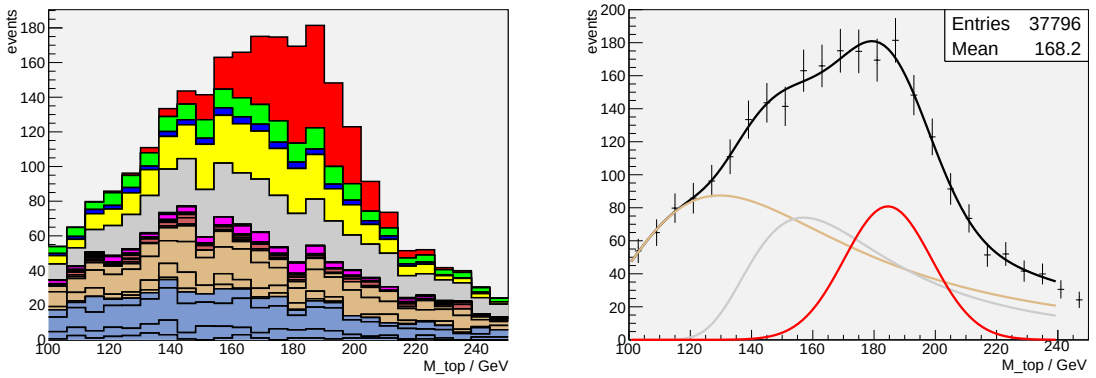

Figure 6.6: The distributions of the 3-jet mass for JES scaling of -10% (a) and +10% (b) and the fits used for approximation for a simulated top mass of 172.5 GeV

The linear dependence on the JES is also visible for the 2-jet mass plotted in Figure 6.8. The effect is again visible that lower simulated top masses result in lower reconstructed W masses due to the event selection process, as described in Section 6.3.2, especially for the sample with $m_{\text{top}} = 160$ GeV.

Simulated m_{top} [GeV]	JES -10%	JES -5%	JES ±0	JES +5%	JES +10%
160	67.3 ± 1.0	71.1 ± 1.1	75.3 ± 1.6	77.9 ± 1.5	81.9 ± 1.1
170	68.7 ± 0.9	72.3 ± 0.9	76.6 ± 1.1	80.7 ± 1.2	84.8 ± 1.3
172.5	70.2 ± 0.9	73.0 ± 1.1	77.1 ± 1.2	80.8 ± 1.4	84.9 ± 1.3
180	71.1 ± 1.0	74.4 ± 1.0	78.6 ± 1.1	82.4 ± 1.1	86.0 ± 1.2
190	71.0 ± 1.2	74.6 ± 1.4	78.1 ± 1.4	82.8 ± 1.3	85.6 ± 1.9

Table 6.6: Reconstructed 2-jet masses (in GeV, with statistical errors) for the different $t\bar{t}$ Monte Carlo samples and JES variations

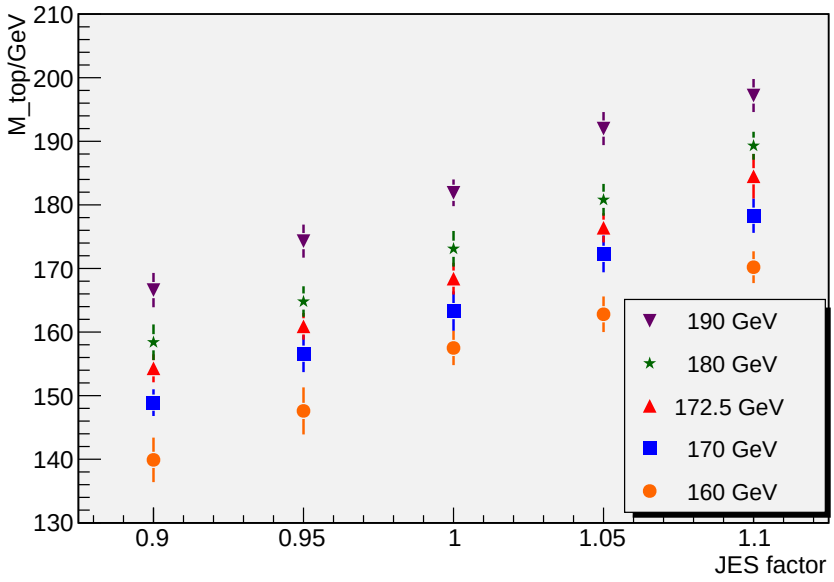

Figure 6.7: The 3-jet mass for different mass points and JES variations

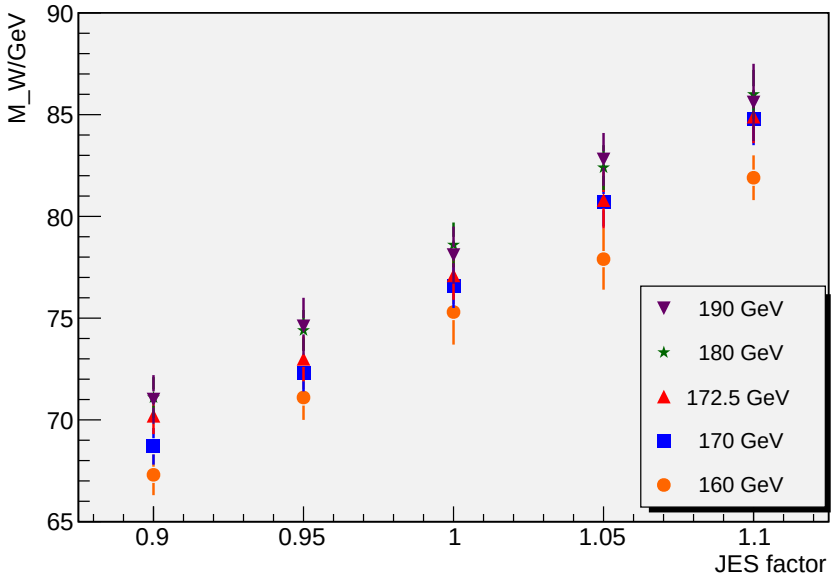

Figure 6.8: The 2-jet mass for different mass points and JES variations

6.4.3 Results for Top Quark Mass

With the analysis behaving as expected under an altered Jet Energy Scale, the value of the re-scaled top mass $m_{\text{top}} = \frac{m_{3-\text{jet}}}{m_{2-\text{jet}}} \cdot m_{\text{W,PDG}}$ can be calculated for each combination of the top mass and JES variations. The results are shown in Table 6.7 and Figure 6.9.

Generally the statistical errors are higher than for the 3-jet mass because the errors from both fits (i.e. on the 2-jet and on the 3-jet mass) have to be taken into account. Although the errors for the signal events are correlated (but not fully correlated as the energy of the b quark jet is only in-

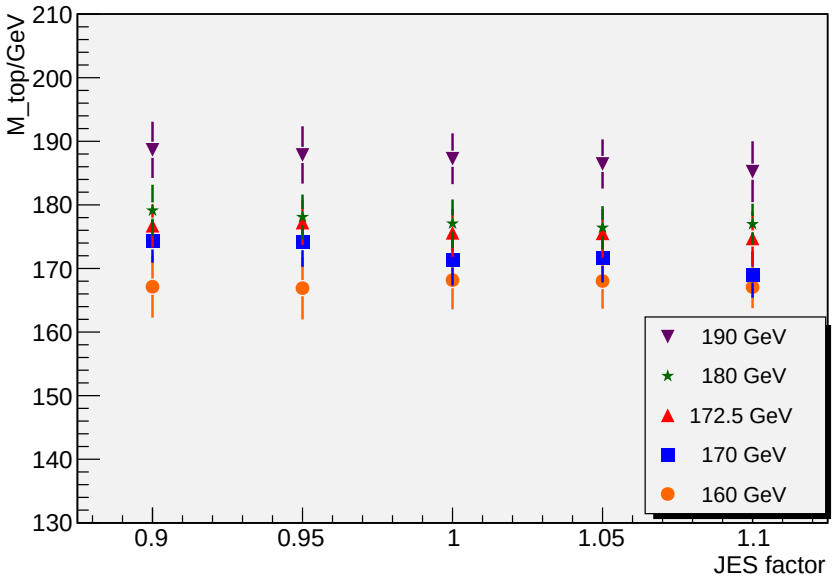

Figure 6.9: The final results for the top masses for the different mass points and JES variations

Simulated m_{top} [GeV]	JES -10%	JES -5%	JES ±0	JES +5%	JES +10%
160	167.1 ± 4.9	166.9 ± 4.9	168.2 ± 4.6	168.0 ± 4.3	167.1 ± 3.3
170	174.3 ± 3.4	174.1 ± 3.9	171.4 ± 4.1	171.7 ± 3.9	169.0 ± 3.6
172.5	176.7 ± 3.4	177.2 ± 3.5	175.6 ± 3.8	175.5 ± 3.8	174.7 ± 4.3
180	179.1 ± 4.0	178.1 ± 3.5	177.1 ± 3.8	176.4 ± 3.4	177.0 ± 3.2
190	188.7 ± 4.4	187.9 ± 4.5	187.3 ± 4.0	186.4 ± 3.9	185.2 ± 4.8

Table 6.7: Reconstructed top quark masses (in GeV, with statistical errors) for the different $t\bar{t}$ Monte Carlo samples and JES variations with rescaling applied

cluded in the 3-jet mass), this cannot be assumed for the combinatorial and physical background – after all, the shape of the background is approximated with different curves for $m_{2-\text{jet}}$ and $m_{3-\text{jet}}$. Because the background is significantly higher than the signal region, the overall correlation is expected to be small; hence, as a conservative estimate, uncorrelated errors are assumed here.

In contrast, a big part of the systematic errors cancels out in the calculation, namely the linear scaling of the JES and a possible bias towards lower or higher top quark masses from the event selection and reconstruction processes.

6.5 Calibration Curve for the Top Quark Mass Result

For the sample with $m_{top} = 160$ GeV, the reconstructed masses are generally around 8 GeV too high. This is a result of the fit for the W mass being too low as described above. On the other end of the spectrum, the mass is reconstructed too low for high simulated masses. This systematic effect, mainly caused by the selection of events, of the analysis can be compensated with a calibration curve for m_{top}. The reconstructed mass for the different simulated mass points, averaged over all

JES variations, are listed in Table 6.8. For the errors on these average masses it has been taken into consideration that the errors in Table 6.7 are correlated.

Simulated m_{top} [GeV]	average reconstructed m_{top} [GeV]
160.0	167.4 ± 4.2
170.0	172.2 ± 3.8
172.5	176.1 ± 3.8
180.0	177.4 ± 3.6
190.0	187.1 ± 4.2

Table 6.8: Reconstructed top quark masses (in GeV, with statistical errors) for the different $\bar{t}t$ Monte Carlo, averaged over the JES variations

Figure 6.10 shows these average values plotted against the simulated m_{top}, and a linear function to approximate the data. This function is

$$m_{\text{reco}} = 147.7\,\text{GeV} + 0.63 \cdot (\text{m}_{\text{true}} - 172.5\,\text{GeV})$$

where m_{reco} is the top quark mass found in the analysis with the method described above, and m_{true} the true top quark mass (the simulated mass for the Monte Carlo study). The final calibration function is then

$$m_{\text{true}} = 1.59 \cdot m_{\text{reco}} - 104.8\,\text{GeV}.$$

The statistical error on the reconstructed mass before the calibration is increased by the factor of 1.59, the slope of the calibration function. With an average value of 3.9 GeV from Table 6.8, the total statistical uncertainty is

$$(\Delta m_{\text{top}})_{\text{stat}} = 6.2\,\text{GeV}.$$

or 3.6% for the central mass point.

A conservative estimate of the remaining systematic error on the Jet Energy Scale is half of the maximum distance between two reconstructions (for different JES scaling factors) of the same simulated mass point. This is, for the sample with $m_{\text{top}} = 170\,\text{GeV}$,

$$(\Delta m_{\text{top}})_{\text{JES}} = \frac{174.3 - 169.0}{2}\,\text{GeV} = 2.7\,\text{GeV},$$

corresponding to a relative uncertainty of 1.6%.

6.6 The Effect of B-Tagging on the Measurement

The most promising feature to reduce both the combinatorial and the physical background is b-tagging. Once reliable algorithms are in place the b-tags can be used to effectively suppress W + Jets and QCD multijet events, and to make the event reconstruction easier. B quark jets are not assigned to the light quarks from the W decay, so the number of possible assignments is reduced to six when one jet is b-tagged and to two when both b quark jets are tagged.

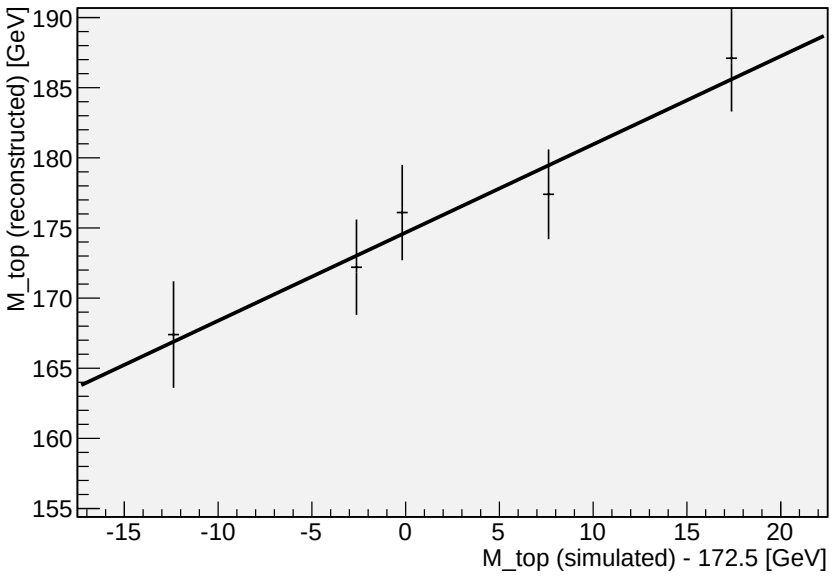

Figure 6.10: Average reconstructed top quark mass for the different JES scaling factors, plotted against the simulated value

At the time of writing no physical background Monte Carlo samples with enabled b-tagging were available for a simulated centre-of-mass energy of 10 TeV. But it can be estimated that the dominant background process, W + Jets, will be reduced by a factor of about 50-100 when two b-tags are required [32, 38], and by a factor of about 20 with a requirement of at least one b-tag [38].

Regarding the reduction of the combinatorial background, the signal efficiency and purity achieved with a cut on one b-tag and two b-tags, respectively, are listed in Table 6.9. Here a b-tagging efficiency of about 40% is assumed.

b-tags	efficiency (preselection)	efficiency (preselection + TMVA)	top + W purity
0	17.7%	13.2%	25.2%
1	11.3%	7.1%	43.1%
2	2.8%	1.3%	65.8%

Table 6.9: Efficiency and purity of cuts on b-tags for the $t\bar{t}$ sample with m_{top} = 172.5 GeV

The impact on the combinatorial background is instantly visible in Figure 6.11. For one b-tag, the signal peak is now by a factor of about 3 higher than the combinatorial background, for two b-tags this value increases to about 7. A much more precise fit is thus possible.

However, more data is needed for the higher statistical uncertainty, caused by the lower selection efficiency, not to outweigh the benefits of a clearer $t\bar{t}$ signal. In particular, a cut on two b-tags will only make sense once several hundred pb^{-1} of data were taken at ATLAS. Requiring at least one b-tagged jet might improve the results of the measurements once the tagging algorithms are commissioned, even with only 100 pb^{-1} of data, because the higher signal purity compensates for the lower efficiency. It has to be considered, though, that the use of b-tagging introduces new systematic uncertainties yet unknown.

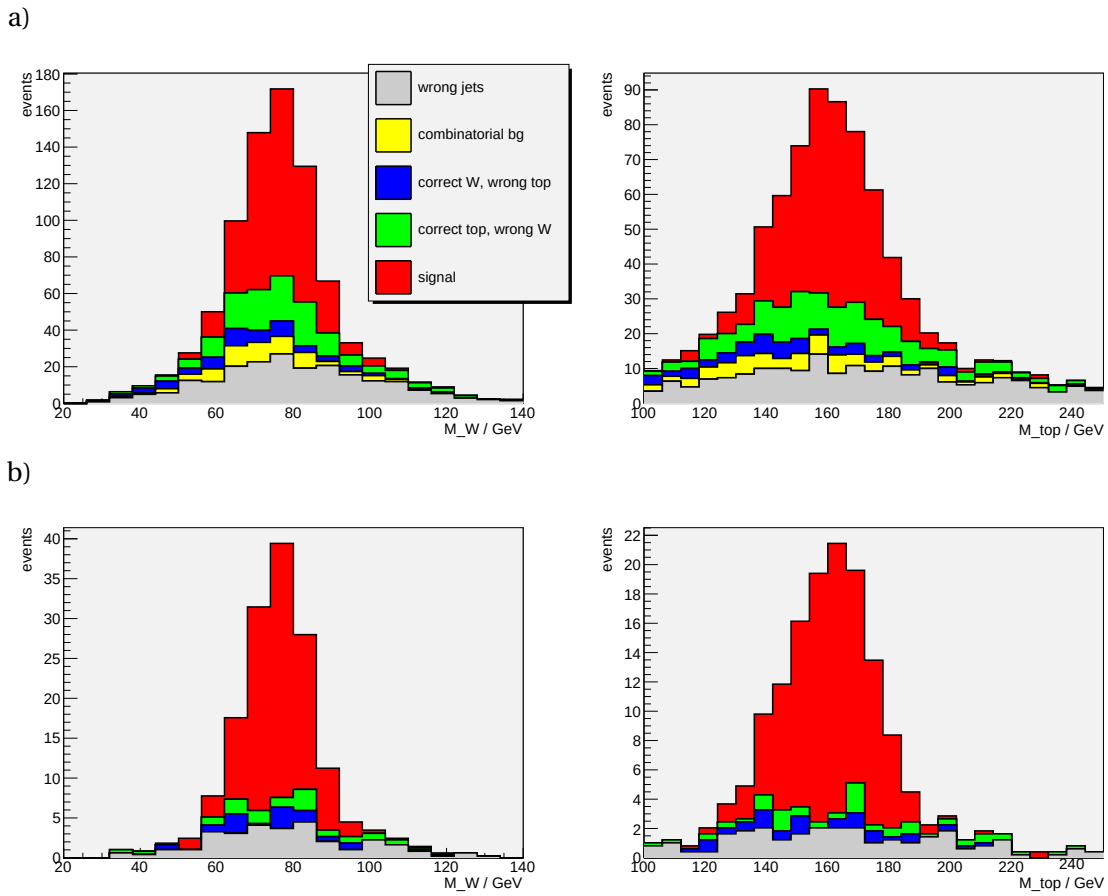

Figure 6.11: Distributions of the 2-jet (left) and 3-jet mass (right) with a requirement of at least one b-tag (a) and two b-tags (b) for a simulated m_{top} of 172.5 GeV; $t\bar{t}$ processes only, no physical background; scaled to 100 pb^{-1}

6.7 QCD Multijet Background

Even though no detailed Monte Carlo study can be performed on the QCD multijet background (see Section 4.3.3), a qualitative estimate of its shape and height can be given. For this purpose Monte Carlo sample from private production are used [30, 39], with a simulated fake rate for electrons (i.e. the probability that a jet is misinterpreted as an electron) of about 1‰. The events were produced for a centre-of-mass energy of $\sqrt{s} = 14$ TeV; the influence of a lower beam energy on the shape and cross section of the background has yet to be studied. The distribution of the 3-jet mass for the QCD multijet events and the $t\bar{t}$ events for the sample with $m_{top} = 172.5$ GeV (at $\sqrt{s} = 10$ TeV) are shown in Figure 6.12.

Note that the uncertainty on the fake rate is high, and that the Monte Carlo statistics is not sufficient to allow for a quantitative analysis of the QCD multijet background. Nevertheless it is apparent that the distribution of the 3-jet mass in the QCD sample is similiar to that of the W + Jets sample, so QCD multijets can be included in the Landau fit for the physical background. The background reduction is sufficient for an early analysis, even without the use of b-tagging. Efforts to estimate the QCD multijet background and its influence on the top quark mass measurement will be made once the experiment is running, using real data.

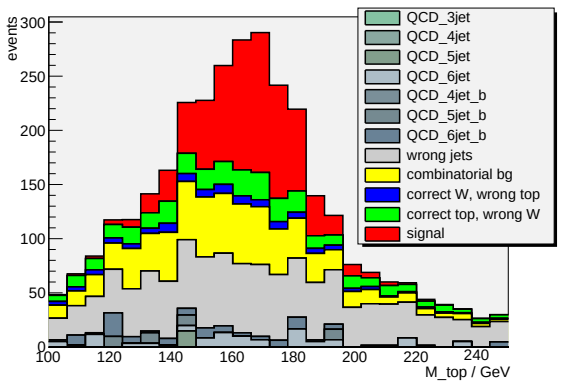

Figure 6.12: The distributions of the 3-jet mass for $t\bar{t}$ signal and QCD multijet background

Chapter 7

Conclusion

When the Large Hadron Collider (LHC) will start colliding protons later this year, a first run of data taking at a centre-of-mass energy of 10 TeV (which will be increased to 14 TeV at a later stage) is planned to yield an integrated luminosity of $\int \mathscr{L} \mathrm{d}t = 200\,\mathrm{pb}^{-1}$. With a production cross section for top pairs of about 400 pb the LHC can be considered a "top quark factory" even at the lower beam energy in the first months, and will thus provide a great opportunity to study top quark physics.

With the first collisions at the LHC, the ATLAS detector will begin its operation as well. Naturally the commissioning and calibration of all its components will take some time to complete, and in the mean time high systematic uncertainties have to be assumed for the measurements.

This study shows that even under the conditions of the first run of the LHC a rediscovery of the top quark and an early determination of its mass is still possible. For this purpose a scenario with relatively low statistics ($\int \mathscr{L} \mathrm{d}t = 100\,\mathrm{pb}^{-1}$) and an uncertainty of 10% on the most important measurement – the jet energies and momenta – is considered; more sophisticated features of ATLAS detector, like bottom quark jet tagging and the determination of the missing transverse energy, are omitted as their performance for early data is unknown.

To meet the challenge of low statistics, together with the high combinatorial background that arises from the difficulties of the event reconstruction without the use of b-tagging, an artificial neural network is used for the jet assignments in the reconstruction to achieve a better signal efficiency and background suppression than possible when relying on kinematic and geometric cuts. That way the signal significance is raised by over 30%.

The determination of the top quark mass is performed in the semileptonic decay channel. The masses of the W boson and top quark from the hadronic decay are determined separately as the 2-jet and 3-jet masses, respectively. To cancel out a possible scaling factor on the jet energies and momenta in early data, the top quark mass is rescaled with the W boson mass given by the Particle Data Group, $m_{\mathrm{W,PDG}} = 80.4\,\mathrm{GeV}$ [2]. This is accomplished by calculation of m_{top} as

$$m_{\mathrm{top}} = \frac{m_{3-\mathrm{jet}}}{m_{2-\mathrm{jet}}} \cdot m_{\mathrm{W,PDG}}.$$

As a final step a calibration curve for m_{top} is given to compensate for systematic effects of the event selection and reconstruction process. The resulting uncertainty on the top quark mass when determined with this procedure, assuming an uncertainty of 10% on the Jet Energy Scale (JES) and

an integrated luminosity of $100\,\mathrm{pb}^{-1}$, is

$$\frac{\Delta m_{\mathrm{top}}}{m_{\mathrm{top}}} = \pm 3.6\%\,(\mathrm{stat}) \pm 1.6\%\,(\mathrm{JES}).$$

The statistical uncertainty outweighs the systematic uncertainty on the JES; in effect, for the first run of the LHC, the limiting factor on the precision of the measurement will be the amount of data taken rather than the calibration of the Jet Energy Scale. However, the influence of other sources of systematic uncertainty, for example the cross section of the QCD multijet background and the electron fake rate, has to be estimated once the experiment is running.

It can be concluded that, in this scenario, a first measurement of the top quark mass is indeed possible with the first data taken at the ATLAS detector, and a precision of about 4% is achievable.

Bibliography

[1] The Tevatron Electroweak Working Group, for the CDF, and D0 Collaborations. Combination of CDF and D0 Results on the Mass of the Top Quark. 2009, 0903.2503.

[2] C. Amsler et al. Review of particle physics. *Physics Letters*, B667, 2008.

[3] D. Griffiths. *Introduction to elementary particles*. John Wiley & Sons, 1987.

[4] S. W. Herb et al. Observation of a dimuon resonance at 9.5-GeV in 400-GeV proton - nucleus collisions. *Phys. Rev. Lett.*, 39:252–255, 1977.

[5] F. Abe et al. Observation of top quark production in $\bar{p}p$ collisions. *Phys. Rev. Lett.*, 74:2626–2631, 1995, hep-ex/9503002.

[6] S. Abachi et al. Observation of the top quark. *Phys. Rev. Lett.*, 74:2632–2637, 1995, hep-ex/9503003.

[7] The ATLAS Collaboration. Expected Performance of the ATLAS Experiment. *ATLAS Communications*, CERN-OPEN-2008-020:386–396, 2008.

[8] S. Moch and P. Uwer. Theoretical status and prospects for top-quark pair production at hadron colliders. *Phys. Rev. D*, 78:034003, 2008.

[9] L. Evans and P. Bryant (eds.). LHC Machine. *JINST*, 3:S08001, 2008.

[10] R. Adolphi et al. The CMS experiment at the CERN LHC. *JINST*, 0803:S08004, 2008.

[11] S. Vecchi. The LHCb experiment and its expected physics performance. *Nucl. Phys. Proc. Suppl.*, 185:213–219, 2008.

[12] P. Crochet. The ALICE experiment at the LHC. *Phys. Part. Nucl.*, 39:1074–1081, 2008.

[13] ATLAS Collaboration. ATLAS inner detector: Technical design report. vol. 1. CERN-LHCC-97-16.

[14] A. Airapetian et al. ATLAS calorimeter performance. CERN-LHCC-96-40.

[15] ATLAS Collaboration. ATLAS muon spectrometer: Technical design report. CERN-LHCC-97-22.

[16] G. Duckeck (ed.) et al. ATLAS computing: Technical design report. CERN-LHCC-2005-022.

[17] S. Frixione and B.R. Webber. Matching NLO QCD computations and parton shower simulations. *JHEP 0206*, 029, 2002, hep-ph/0204244.

[18] S. Frixione and B. R. Webber. The MC@NLO 3.3 event generator. 2006, hep-ph/0612272.

[19] T. Sjostrand, S. Mrenna, and P. Skands. PYTHIA 6.4 physics and manual. *JHEP*, 05:026, 2006, hep-ph/0603175.

[20] G. Marchesini et al. HERWIG: A Monte Carlo event generator for simulating hadron emission reactions with interfering gluons. Version 5.1 - April 1991. *Comput. Phys. Commun.*, 67:465–508, 1992.

[21] S. Agostinelli et al. Geant4: A simulation toolkit. *Nucl. Instrum. Meth.*, A506:250–303, 2003.

[22] S. Dean and P. Sherwood. ATLFAST - the ATLAS Fast Simulation Package. `http://www.hep.ucl.ac.uk/atlas/atlfast/`, 2007.

[23] A. Shibata. TopView - ATLAS top physics analysis package. *ATLAS Public Note*, ATL-SOFT-PUB-2007-002, 2007.

[24] R. Brun and F. Rademakers. ROOT - An Object Oriented Data Analysis Framework. Proceedings AIHENP'96 Workshop, Lausanne, Sep. 1996, Nucl. Inst. and Meth. in Phys. Res. A 389 (1997) 81-86. See also `http://root.cern.ch/`.

[25] The ATLAS Collaboration. The ATLAS Experiment at the CERN Large Hadron Collider. *J. Instrum.*, 3:S08003, 2008.

[26] L. Vacavant. b-tagging algorithms and performance in ATLAS. *Proceedings of Science*, ATL-PHYS-PROC-2009-023, 2009.

[27] CDF Collaboration. Measurement of the Top Quark Mass in the Dilepton Channel using a Matrix Element Method and Neuroevolution Selection with 2.0 fb^{-1}. 2007, 0712.2864.

[28] A. Abulencia et al. Measurement of the top quark mass using template methods on dilepton events in proton antiproton collisions at $\sqrt{s}$ = 1.96-TeV. *Phys. Rev.*, D73:112006, 2006, hep-ex/0602008.

[29] N. Konstantinidis et al. The Atlantis event visualisation program for the ATLAS experiment. *Interlaken 2004, Computing in high energy physics and nuclear physics*, pages 361–364, 2005.

[30] R. Mameghani. *Semi- and Dileptonic Top Pair Decays at the ATLAS Experiment.* PhD thesis, Ludwig-Maximilians-Universität München, 2008.

[31] G. P. Salam. A Practical Seedless Infrared Safe Cone Algorithm. 2007, 0705.2696.

[32] P. G. Cavalleri. Top quark mass measurement with ATLAS. *ATLAS Communications*, ATL-COM-PHYS-2008-266, 2008.

[33] E. Cogneras and D. Pallin. Top Mass measurement in the 2 b-tagged semileptonic $t\bar{t}$ channel. *ATLAS Communications*, ATL-COM-PHYS-2008-44, 2008.

[34] T. Mitchell. *Machine Learning.* McGraw Hill, 1997.

[35] M. Ester and J. Sander. *Knowledge Discovery in Databases.* Springer, 2000.

[36] A. Höcker et al. TMVA - Toolkit for Multivariate Data Analysis. Technical Report physics/0703039. CERN-OPEN-2007-007, 2007.

[37] F. James and M. Roos. Minuit: A System for Function Minimization and Analysis of the Parameter Errors and Correlations. *Comput. Phys. Commun.*, 10:343–367, 1975.

[38] A.-I. Etienvre et al. Top quark mass measurement in the lepton plus jets channel with a kinematic fit on the full final state. *ATLAS Communications*, ATL-PHYS-INT-2008-021, 2008.

[39] M. Lambacher, O. Biebel, and F. Fiedler. Generation of QCD multijet background events with ALPGEN version 2.03 and ATLFAST version 11.0.41. *ATLAS Communication*, ATL-PHYS-INT-2007-007, 2007.

Acknowledgements

I would like to thank everyone who made this thesis possible with their help and support, and in particular:

- Prof. Otmar Biebel for his supervision of my thesis, his input and his encouragement, and for all the time he took to discuss my questions in spite of his full schedule,
- Prof. Faessler for the second evaluation of my thesis,
- Prof. Dorothee Schaile for the enjoyable work environment at her institute,
- Dr. Raphael Mameghani for his invaluable help in the preparation and realisation of the analysis, for his support with his expertise in top quark physics, and for proof-reading my thesis,
- Dr. Johannes Elmsheuser for his support with the grid computing tools, and Dr. Marie-Hélène Genest for the production of the ntuples files,
- Markus Lichtnecker, Jonas Will, Dr. Raphael Mameghani, Michael Wichmann and Julien de Graat for fun conversations beyond physics, making the time at the institute entertaining,
- everyone else working at the institute not already mentioned for contributing to inspiring discussions and the enjoyable atmosphere in the work group: Stefanie Adomeit, Sebastian Becker, Dr. Philippe Calfayan, Dr. Günter Duckeck, Johannes Ebke, Albert Engl, Herta Franz, Dr. Cristina Galea, Alexander Grohsjean, Dr. Petra Haefner, Dr. Ralf Hertenberger, Dr. John Kennedy, Christian Kummer, Dr. Gernot Krobath, Thomas Langer, Dr. Tariq Mahmoud, Dr. Doris Merkl, Christoph Anton Mitterer, Thomas Müller, PD Dr. Thomas Nunnemann, Dr. Felix Rauscher, Benjamin Ruckert, Dr. Michiel Sanders, Dr. Cedric Serfon, PD Dr. Raimund Ströhmer, Attila Varga and Dr. Rod Walker;
- my fellow student and friend Paul Käufl for sharing the joys and struggles of the degree, and for proof-reading my thesis,
- my family, for their continued support throughout my time at university and
- Franziska, for her encourangement and too many more reasons to list here.

Erklärung

Ich erkläre hiermit, dass ich meine Diplomarbeit mit dem Titel

**„Early Measurement of the Top Quark
Mass at the ATLAS Experiment“**

selbständig verfasst sowie keine anderen als die angegebenen Quellen und Hilfsmittel benutzt habe.

München, 31. März 2009

_____

(Klaus Herrmann)